Spatio-Temporally Skewed Activation of PD-1$^+$ T Cells after Epstein Barr Virus Infection and Tumor Development in Long-Term Fully Humanized Mice

Simon Danisch, Constanze Slabik, Angela Cornelius, Manuel Albanese, Takanobu Tagawa, Yen-Fu Adam Chen, Nicole Krönke, Britta Eiz-Vesper, Stefan Lienenklaus, Andre Bleich, Sebastian J. Theobald, Andreas Schneider, Arnold Ganser, Constantin von Kaisenberg, Reinhard Zeidler, Wolfgang Hammerschmidt, Friedrich Feuerhake, Renata Stripecke

PII: S0002-9440(18)30470-X

DOI: https://doi.org/10.1016/j.ajpath.2018.11.014

Reference: AJPA 3056

To appear in: *The American Journal of Pathology*

Received Date: 4 June 2018

Revised Date: 26 October 2018

Accepted Date: 6 November 2018

Please cite this article as: Danisch S, Slabik C, Cornelius A, Albanese M, Tagawa T, Adam Chen Y-F, Krönke N, Eiz-Vesper B, Lienenklaus S, Bleich A, Theobald SJ, Schneider A, Ganser A, von Kaisenberg C, Zeidler R, Hammerschmidt W, Feuerhake F, Stripecke R, Spatio-Temporally Skewed Activation of PD-1$^+$ T Cells after Epstein Barr Virus Infection and Tumor Development in Long-Term Fully Humanized Mice, *The American Journal of Pathology* (2019), doi: https://doi.org/10.1016/j.ajpath.2018.11.014.

Spatio-temporally skewed activation of PD-1^+ T cells after Epstein Barr virus infection and tumor development in long-term fully humanized mice

Simon Danisch[1,2], Constanze Slabik[1,2], Angela Cornelius[1,2], Manuel Albanese[3], Takanobu Tagawa[3], Yen-Fu Adam Chen[3], Nicole Krönke[4], Britta Eiz-Vesper[5], Stefan Lienenklaus[6], Andre Bleich[6], Sebastian J. Theobald[1,2], Andreas Schneider[1,2], Arnold Ganser[1], Constantin von Kaisenberg[7], Reinhard Zeidler[3,8], Wolfgang Hammerschmidt[3], Friedrich Feuerhake[4,9], Renata Stripecke[1,2]

[1] Department of Hematology, Hemostasis, Oncology and Stem Cell Transplantation, Hannover Medical School, Hannover, Germany.

[2] Laboratory of Regenerative Immune Therapies Applied, Excellence Cluster REBIRTH and German Centre for Infection Research (DZIF), Partner site Hannover, Hannover, Germany.

[3] Research Unit Gene Vectors, Helmholtz Zentrum München, German Research Center for Environmental Health and German Centre for Infection Research (DZIF), Partner site Munich, Munich, Germany.

[4] Institute of Pathology, Hannover Medical School, Hannover, Germany.

[5] Institute for Transfusion Medicine, Hannover Medical School, Hannover, Germany

[6] Institute for Laboratory Animal Science, Hannover Medical School, Hannover, Germany.

[7] Department of Obstetrics, Gynecology and Reproductive Medicine, Hannover Medical School, Hannover, Germany

[8] Department of Otorhinolaryngology, Klinikum der Universität and German Centre for Infection Research (DZIF), Partner site Munich, Munich

[9] Institute for Neuropathology, University Clinic Freiburg, Freiburg, Germany

Footnote: S.D. and C.S. contributed equally and W.H., F.F., and R.S. contributed equally as senior authors.

Corresponding Author: Renata Stripecke, Carl-Neuberg-Str.1, 30625 Hannover, Germany

Phone: +49 511/ 532-6999, Fax: +49 511/ 532- 6975

Mail: stripecke.renata@mh-hannover.de

Short running title: EBV tumors and $CD8^+$ PD-1^+ T cell skewing

Number of text pages: 37. Number of tables: 2+1. Number of figures: 10+2. Movie: 1.

Funding: Supported by grants of the German Center for Infections Research (DZIF-TTU07.803) and German Research Council (DFG/ SFB738 Project A6; DFG/ REBIRTH Unit 6.4) to R.S; grants of the Deutsche Forschungsgemeinschaft [grant numbers SFB1064/TP A04 and TP A13, SFB-TR36/TP A04], Deutsche Krebshilfe [grant numbers 107277, 109661] to W.H.; National Cancer Institute [grant number CA70723] and a personal grant to T.T. from Deutscher Akademischer Austauschdienst (DAAD, Studienstipendien für ausländische Graduierte aller wissenschaftlichen Fächer); grants of the German Federal Ministry of Education and Research (BMBF), by Projektträger Jülich (PTJ), Grant #031B0006C “ILUMINATE” and Projektträger DLR, Grant #01ZX1608A (“SYSIMIT”) to F.F. S.T. received a RegSci PhD fellowship.

Disclosures: R.S. received honoraria as a lecturer in conferences from The Jackson Laboratory, which commercially distributes the NRG mice.

Abstract

Humanized mice developing functional human T cells endogenously and capable of recognizing cognate HLA-matched tumors are emerging as relevant models for studying human immuno-oncology *in vivo*. Here, mice transplanted with human CD34$^+$ stem cells and bearing endogenously-developed human T cells for more than 15 weeks were infected with an oncogenic recombinant Epstein Barr virus (EBV), encoding enhanced firefly luciferase (fLuc) and green fluorescent protein. EBV-fLUC was detectable one week after infection by non-invasive optical imaging in the spleen, from where it spread rapidly and systemically. EBV infection resulted into a pronounced immunological skewing regarding the expansion of CD8$^+$ T cells in the blood outnumbering the CD4$^+$ T and CD19$^+$ B cells. Furthermore, within 10 weeks of infections, mice developing EBV-induced tumors had significantly higher absolute numbers of CD8$^+$ T cells in lymphatic tissues than mice controlling tumor development. Tumor outgrowth was paralleled by an up-regulation of the programmed cell death receptor 1 (PD-1) on CD8$^+$ and CD4$^+$ T cells, indicative for T-cell dysfunction. Histopathological examinations and *in situ* hybridizations for EBV in tumors, spleen, liver, and kidney revealed foci of EBV-infected cells in perivascular regions in close association with PD-1$^+$ infiltrating lymphocytes. The strong spatio-temporal correlation between tumor development and the T cell dysfunctional status seen in this viral oncogenesis humanized model replicates observations obtained in the clinical setting.

Introduction

In recent years, immunotherapeutic approaches with immune checkpoint inhibitors showed unprecedented and long-lasting responses even in cancer patients with advanced disease [1]. Nivolumab, an antibody blocking the programmed cell death receptor (PD)-1, inhibited tumor immune evasion in patients with relapsed or refractory Hodgkin's lymphoma (HL) with remarkable 87% objective responses [2]. Consequently, a promising rich pipeline of novel therapeutic antibodies and innovative combination therapies targeting checkpoint molecules expressed on T cells and/or tumor cells is currently being developed to abrogate tumor-induced immunosuppression. A limitation in this preclinical field is testing these human-specific antibodies *in vivo*, since the immune responses obtained in mice or non-human-primates sometimes do not predict what can be observed in immunologically distinct and genetically heterogeneous human beings. Therefore, novel *in vivo* models suitable for validating these immunotherapies are warranted to accelerate their translation to patients. Mice reconstituted with a human immune system, also called “humanized mice”, have emerged in the past decade as an important pre-clinical platform for *in vivo* efficacy testing of human-specific therapeutic drugs [3]. Several groups have reported that the use of $CD34^+$ human hematopoietic stem cell transplantation (huHSCT) into severely immune deficient mouse strains such as non-obese diabetic/severe combined immune deficient (NOD/*SCID)* $IL2rg^{null}$ (NSG) [4], NOD $Rag1^{null}$ $IL2rg^{null}$ (NRG)[5], [6], or BALB/c-$Rag2^{null}$ $Il2rg^{null}$ (BRG)[7] mice resulted in consistent human hematopoietic engraftment in the bone marrow and development of human lymphocytes in lymphatic tissues. Remarkably, highly xeno-reactive human T cells seem to be functionally depleted in the thymus, so that endogenously developing human mature T cells can persist long-term for several months up to nearly a year after huHSCT with only sporadic occurrence of graft-versus-host disease [6], [8]. Concurrently, patient-derived tumor xenograft (PDX) cancer models transplanted into NSG mice showed that these *in vivo* models can be predictive of clinical outcomes [9]. PDX mouse models combined with humanized immune systems could further enable their use for testing immunotherapies. Recently, Wang et al showed that after huHSCT, NSG humanized mice transplanted with PDX cells matched to a few but not all of the class I human leukocyte antigens (HLAs) developed tumors [10]. Moreover, treatment with an anti–PD-1 antibody (pembrolizumab) showed significant tumor growth inhibition. Inherent limitations of PDX models surgically grafted into humanized mice include i) HLA mismatch between stem cell donor(s) and tumors, and ii) sequential loss of the original tumor microenvironment (TME) during tumor outgrowth in the mouse. Both problems can be overcome in an *in vivo* model of virus-induced hematological tumors, where the malignant cells and the immune system carry the same HLAs and tissue antigens and the neoplasm development induces its own individual TME. Epstein Barr virus (EBV) is a type 1 carcinogen that is directly associated with the development of human B cell neoplasms [11]. EBV infection models in humanized mice six to 10 weeks after huHSCT have been described previously [12], [13], [14]. Nevertheless, at this early time point, the human immune reconstitution consists of an insufficient development, maturation, and egress of human lymphocytes from primary lymphatic tissues to the periphery and it is thus not advanced enough to counteract the virus and explosive outgrowth of EBV-induced tumors [15], [16], [17], [18]. Indeed, one study by Lee et al elegantly showed that the timepoint of EBV infection after huHSCT critically affected the burden and types of developing tumors [19]. Thus, consistent outgrowth of tumors resembling non-Hodgkin lymphomas (NHL) developed when EBV infection occurred at eight weeks after huHSCT (when immature B cells predominated, and T cells were lacking), whereas fewer tumors developed and resembled the TME of HL when mice were infected 15 weeks after huHSCT (at the timepoint when T cell development and maturation can be observed in this model).

These HL-like tumors were histologically more complex and contained Hodgkin's Reed–Sternberg (HRS)-like cells [19]. These observations by Lee et al suggested a link between the level of reconstitution of the human adaptive immunity in humanized mice and the shaping of the tumor and, in turn, the establishment of an immunosuppressive TME. Here, we hypothesized that EBV infection and tumor progression in long-term humanized mice would shape the activation of T cell lineages and induce PD-1 up-regulation. The data reveal that most mice infected with EBV 15 to 17 weeks after huHSCT and analyzed 10 weeks later did not develop macroscopically detectable tumors, but nevertheless showed a skewed CD8$^+$ T cell expansion in several lymphatic tissues as compared with non-infected mice. In animals showing tumors caused by EBV infection, an even more substantial expansion of CD8$^+$ PD-1$^+$ T cells was observed in tumor tissues. Histopathology analyses of adjacent tissue, combined with *EBER in situ* hybridization, characteristically revealed recurrent patterns of spatial organization with foci of EBV infected cells in close association with PD-1$^+$ infiltrating lymphocytes, often in perivascular regions. Therefore, long-term humanized mice infected with EBV demonstrated a range of dynamic and vigorous interplay between tumor development and the immune system in multiple organs. This working model recapitulates clinical findings of chronic and acute EBV infection and could be used to study systemic T cell activation and local responses in the TME at different stages of organ involvement and tumor formation.

Material and Methods

Ethics Statement

All subjects donating cord blood provided written informed consent. This study was approved by the Ethics Committee of Hannover Medical School.

Generation of EBV engineered strains

EBV-B95.8/GFP is a genetically modified strain (also known as 2089-EBV) derived from the B95-8 strain [20, 21] and was amplified in HEK293 cells as described [22]. EBV-B95.8/fLuc2 was derived from EBV-B95.8/GFP strain and contains a codon-optimized firefly luciferase (fLuc) cDNA (*luc2*, Genscript Biotech, Piscataway Township, NJ) coupled to a preceding T2A element and engineered to be expressed downstream of the viral Epstein Barr nuclear antigen 2 (*EBNA2*) gene. The viral genome was constructed using recombinant DNA technologies in a modified *E.coli* DH10B strain [23-25]. The resulting maxi EBV plasmid p6476 was carefully analyzed by restriction enzyme analysis and all relevant genetically modified regions were confirmed by sequencing. The EBV-B95.8/fLuc2 virus was introduced into HEK293 cells, single cell clones were isolated and induced to produce progeny virus. Viral titers were determined and indicated as GFP Raji infectious units (GRU) as previously described [26].

Generation of humanized mice

All experiments involving mice were performed in accordance with the regulations and guidelines of the animal welfare of the State of Lower Saxony (Niedersächsiches Landesamt für Verbraucherschutz und Lebensmittelsicherheit, Dezernat 33/Tierschutz). Four- to 6-week–old NRG mice were originally obtained from The Jackson Laboratory (JAX, Bar Harbor, ME) and bred in-house under pathogen-free conditions. Cord blood (CB) units were obtained after informed consent from donors (mothers at term) and study protocols approved by the Ethics Committee of the Hannover Medical School. Human CD34$^+$ hematopoietic cells were isolated from CB after two rounds of positive selection using immune magnetic beads (Direct CD34 Progenitor Cell isolation Kit, human, MACS Miltenyi Biotec, Bergisch Gladbach, Germany) as described [27]. CD34$^+$/CB units were pretested in a couple of transplanted mice and only those resulting into 20% or higher frequencies of human CD45$^+$ cells in mouse peripheral blood lymphocytes 15 weeks post HSCT were used for further experiments. Prior to HSCT, mice were sublethally irradiated (450 cGy) using a [^{137}Cs] column irradiator (Gammacell 3000 Elan; Best Theratronics, Ottawa, Canada). 4 h after irradiation, 2.0 x 10^5 CD34$^+$ cells were administrated to mice through the tail vein as described [28, 6]. For these experiments, both male and female mice were used.

Analyses of human T and B cell reconstitution in different tissues

Patterns of human T and B cell reconstitution in peripheral blood (BL), spleen (SPL), mesenteric lymph nodes (mLN), peripheral lymph nodes (LN), and bone marrow (BM) were analyzed by flow cytometry essentially as described [28, 6] with minor modifications. Lysis of erythrocytes was performed in 0.83% ammonium chloride/20 mM HEPES, pH 7.2 for 5 min at room temperature, followed by stabilization with cold PBS (Biochrom, Berlin, Germany) and washing. Spleen, peripheral lymph nodes (LN), mesenteric lymph nodes (mLN), and BM cells were isolated and homogenized. Before homogenization the spleen was cut in small pieces and pre-digested with 2 mg/mL Collagenase D (Roche, Mannheim, Germany) and 2 U/mL DNAseI (NEB, Frankfurt, Germany) in RPMI (Thermo Fisher Scientific, Waltham, MA) at 37 °C for 1 to 2 h. Cell suspensions were washed and resuspended in PBS for counting and staining with the following fluorochrome-conjugated monoclonal antibodies: Pacific blue anti-CD45, Alexa Flour® 700 (AF700) anti-CD19, Brilliant violet™ 510 (BV510) anti-CD3, Peridinin chlorophyll (PerCP) antiCD4, Phycoerythrin-Cyanine7 (PC7) anti-CD8, Phycoerythrin (PE) anti PD-1, allophycocyanin (APC) anti CD69, allophycocyanin (APC) anti-CD366 (T cell immunoglobulin mucin or Tim-3, BioLegend, San Diego, CA), allophycocyanin-H7 (APC-H7) anti-CD4 (BD bioscience, Becton Dickinson GmbH, Heidelberg, Germany). Cells were stained for 30 min on ice, washed, fixed with

CellFIX (BD bioscience, Becton Dickinson GmbH, Heidelberg, Germany). Flow cytometric data were acquired using a LSR II flow cytometer (BD Bioscience, Becton Dickinson GmbH, Heidelberg, Germany) or CytoFLEX S (Beckman Coulter, Brea, CA) and analyzed using FlowJo (Version: 10, Tree Star, Ashland, OR). To obtain the absolute cell counts, the total number of viable cells counted after homogenization of the tissues was divided by the percentage of the specific cell population after flow cytometry analyses.

Infection of humanized mice with EBV

After confirmed human hematopoietic engraftment in peripheral blood 15 to 17 weeks after HSCT, mice were randomized based on the levels of T cell reconstitutions between control and EBV-infected groups. For EBV-infections, mice were injected via the tail vein with 10^5 GRU of EBV-B95.8/fLuc2 or EBV-B95.8/GFP diluted in 100 µL PBS. Weight monitoring after infections was performed weekly. Euthanasia was performed if symptoms of distress due to tumor development were detected or 10 weeks post EBV infections.

Optical and CT imaging analyses of EBV-infected mice

Mice infected with EBV-B95.8/fLuc2 were analyzed for luciferase expression using an IVIS SpectrumCT apparatus (PerkinElmer, Waltham, MA). In brief, mice were anaesthetised using Isoflurane. Five min before imaging, 2.5 mg D-Luciferin potassium salt (SYNCHEM, Elk Grove Village, IL) dissolved in 100µL PBS were administered intraperitoneally (i.p.). For 3D reconstruction of the bioluminescent signal, µCT data were acquired at the same time as acquisition of the optical data. Data were analyzed using the LivingImage Software (PerkinElmer, Version: 4.5).

Quantification of EBV by qPCR

DNA was extracted from whole spleen specimens using the DNeasy Blood & Tissue Kit (Qiagen, Venlo, The Netherlands) according to the manufacturer's protocol. Quantification of EBV DNA was performed by amplifying a fragment of the *BALF4* gene using the following primers: forward, 5'-CTTTGGCGCGGATCCTC-3' and reverse 5'-AGTCCTTCTTGGCTAGTCTGTTGAC-3'. Amplification was detected by using the following Taqman probe: 5'-Fam-CATCAAGAAGCTGCTGGCGGCC-Tamra-3'. For reaction, 5µL of DNA was added to 20 µL of Taqman 2x Universal Mastermix (Thermo Fisher Scientific, Waltham, MA) mix containing 2.5µL of each primer (2 µM) and 1µL of Taqman probe (5 µM) and 1.5µL of PCR grade nuclease-free water. PCR reactions were run with the StepOnePlus™ Real time system (Applied Biosystems, Life Technologies, Darmstadt, Germany) using the following cycling conditions: 2 min at 50 °C, 10 min at 95 °C, 40 cycles of 15 s at 95 °C, and 1 min at 56 °C. Data were analyzed using the StepOnePlus™ software (Applied Biosystems, Life Technologies, Version: 2.3).

Detection of IFN-γ–secreting T cells by ELISpot

EBV-specific IFN-γ producing T lymphocytes were enumerated by IFN-γ ELISpot assay as described previously[29]. Briefly, viable mononuclear cells obtained from tissues of humanized mice (n=3 for each cohort) or peripheral blood from EBV-seropositive donors (n=3) or cord blood (n=3) were plated at a density of $2.5x10^5$ cells/well and incubated overnight with 2.5 µg/mL CEF peptide pool as a positive control, ppBZLF1 peptide pool (1 µg/mL pro peptide), and T-activated EBNA3A and BZLF1-protein, respectively (2 µL each, both from Lophius Biosciences, Regensburg, Germany). Untreated cells served as negative control Spot forming units (sfu) were counted and analyzed using the AID iSpot Spectrum Reader (AID, Straßberg, Germany) A spot count at least two times higher than the spot count of the negative control was regarded positive.

Histopathology, immunohistochemistry, and image analysis

Formalin–fixed, paraffin–embedded tissues were sectioned into 3µm thick sections and stained according to standard protocols for Hematotoxilin-Eosin (H&E) and Giemsa. Immunohistochemistry (IHC) using the Benchmark Ultra automated instrument (Ventana/Roche Tissue Diagnostics, Mannheim, Germany) was performed for staining: CD8 (clone C8/144B, Dako, Copenhagen, Denmark), CD4 (clone SP35, Zytomed Systems, Berlin, Germany), PD-1 (MRQ-22 Medac Diagnostika, Wedel, Germany), CD30 (Ber-H2, Dako), and PDL-1 (clone 22C3, Dako). The 3,3'-diaminobenzidine (DAB) – based UltraView detection reagent was used following the manufacturer's recommendations. EBV-infected cells were detected by *in situ* hybridization (ISH) using the *EBER* 1 DNP Probe (Ventana/ Roche, designed to bind to Epstein-Barr Virus-encoded *RNA 1*, *EBER 1*) and the automated Benchmark Ultra instrument. Staining results were evaluated visually, and photographs were taken on the Olympus BX46 microscope. In addition, CD4, CD8, PD-1, and *EBER* staining was evaluated using Mantra Quantitative Pathology Workstation, including the INFORM software (Perkin Elmer, Rodgau, Germany, Version 2.4.1). Three to five visually selected fields of view (FOV) acquired with the 20x objective were subjected to color-deconvolution by multispectral imaging (MSI). The perivascular lymphocytic infiltrate was manually annotated. Computational color deconvolution was used to separate color channels (black/dark blue for ISH, blue for hematoxylin, and DAB/brown CD4, CD8, and PD-1. Segmentation and classification of image objects using the INFORM cell phenotyping tool resulted in accurate detection of *EBER*-positive nuclei (ISH), which were recorded as number of stained nuclei per area (in pixels). The density of immune cells (corresponding to the relative number of CD4, CD8, and PD-1–positive cells by IHC) was estimated regarding positively stained image objects per area (in pixels).

Statistical analyses

For these proof-of-concept experiments, data acquisition was not blinded and sample sizes were not statistically determined prior to experiments. Statistical analysis was performed using the GraphPad Prism software (Graphpad Software Inc., La Jolle, CA, Version: 6 and 7). One-way ANOVA with Tukey post-test for multiple comparisons was used to calculate statistical significance. A P-value of less than 0.05 was considered statistically significant.

Results

Infection of humanized mice with EBV-B95.8/fLuc2 monitored by non-invasive optical imaging analyses and computer tomography shows exponential and systemic EBV burst

Prior to *in vivo* use, the titers of EBV viral batches were tested by *in vitro* infection and immortalization of primary B cells. EBV-transformed lymphoblastoid cell lines (LCLs) showed detectable expression of PD-L1 and PD-1 on the cell surface (**Fig.1A**). Fifteen weeks after huHSCT using CD34$^+$ cells from three individual CB donors, mice were infected via tail vein injection with EBV-B95.8/fLuc2 or EBV/GFP (10^5 GRU). Mice were sacrificed 10 weeks later or earlier if signs of disease became evident (**Fig. 1B**). Optical imaging for tracking the biodistribution of the EBV-B95.8/fLuc2 infections showed a faint bioluminescence signal restricted to the anatomical region of spleen one week after infection, which then increased exponentially until five weeks post infection (**Fig. 1C, D**). At this point, when the bioluminescence signals were very conspicuous, 3-dimensional high resolution optical imaging combined with computer tomography (CT) showed “hotspots” of EBV-infected cells dispersed in regions of the spleen and adjacent lymph nodes (**Fig. 1E, Supplemental Movie S1**). Optical imaging analyses performed after euthanasia and inspection of the organs by optical imaging analyses showed pronounced bio-luminescent signals in spleen, lymph nodes, lungs, liver, and salivary glands (**Fig. 1F**).

EBV-B95.8/GFP infection and tumor development changes the kinetics of human immune cell reconstitution in blood, skewing towards significantly higher frequencies of CD8$^+$ T cells

Mice transplanted with CD34$^+$ cells obtained from several CB donors were used to replicate independent experiments for comparisons between non-infected controls (n=19) and EBV-B95.8/GFP-infected (n=18) **(Table 1)**. Among EBV-infected mice, 8/18 (=44%) developed macroscopically visible tumors in the spleen. For further analyses of the data, EBV-infected mice were then compared with ("EBV-Tumor") or without ("EBV") macroscopic tumors **(Table 1)**. All mice showed detectable hCD45$^+$ cells in the peripheral blood until euthanasia (ie, 25 to 27 weeks after huHSCT), but though control mice consistently showed a gradual reduction in the frequencies of hCD45$^+$ cells over time, EBV-infected mice showed more variable patterns **(Fig. 2A, B)**. Regarding the kinetics of B and T lymphocytes, CD19$^+$ B cells predominated at the time of infection, but their frequencies gradually decreased over time for all groups (**Fig. 2C, D**). Remarkably, this drop was significantly more pronounced at six weeks post-infection for EBV-infected mice compared with controls (control vs EBV; P = 0.0102, control vs EBV-Tumor; P = 0.0007, **Fig. 2D**). Concurrently, EBV-infected mice showed a significantly faster expansion of CD3$^+$ T cells compared to non-infected mice (control vs EBV; P = 0.0165, control vs EBV-Tumor; P = 0.0056, **Fig. 2E**). Whereas the frequency of CD4$^+$ T cells within hCD45$^+$ cells in blood slightly decreased after EBV infection relative to controls (control vs EBV; P = 0.77, control vs EBV-Tumor; P = 0.38, **Fig. 3A, B**), the relative CD8$^+$ T cell frequencies increased significantly and constantly (control vs EBV; *P* = 0.0021, control vs EBV-Tumor; *P* ≤ 0.0001, EBV vs EBV-Tumor; *P* = 0.0072, **Fig. 3A, C**).

EBV-B95.8/GFP infection followed by tumor development significantly stimulates the expansion of CD8$^+$ T cells in lymphatic tissues

Tumor development was associated with higher frequencies of CD8$^+$ T cells within hCD45$^+$ cells in BL and lymphatic tissues (mLN, SPL, and BM) (**Table 2, Fig. 4 A, B, C, E, G**). Nonetheless, in terms of absolute cell counts, the increases were more dramatic in EBV-Tumor mice. These differences amounted to approximately 10-fold relative to controls and 3-fold relative to mice not developing tumors (SPL: control vs EBV; *P* = 0.45, control vs EBV-Tumor; *P* ≤ 0.0001, EBV vs EBV-Tumor; *P* = 0.0023 **Fig. 4D**; LN: control vs EBV; *P* = 0.67, control vs EBV-Tumor; *P* = 0.003, EBV vs EBV-Tumor; *P* = 0.04 **Fig. 4F**; BM: control vs EBV; *P* = 0.45, control vs EBV-Tumor; *P* ≤ 0.0001, EBV vs EBV-Tumor; *P* = 0.0007, **Fig. 4H**). Compared with CD8$^+$ T cells, the increase in the absolute CD4$^+$ T cell counts in EBV-Tumor mice relative to controls or EBV mice without tumors was not so pronounced (**Table 2, Fig.4D, F, H**).

Analyses of PD-1 expression on T cells obtained from different lymphatic tissues

The frequencies of PD-1 expressing CD4$^+$ and CD8$^+$ T cells were analyzed by quantitative flow cytometry (**Fig.5A**). For control mice, the frequencies of PD-1$^+$ CD4$^+$ T and PD-1$^+$ CD8$^+$ T cells were 20% to 40% in mesenteric lymph nodes (mLN) and 85% to 90% in bone marrow (BM) (**Fig.5B, D, Supplemental Table S1**). In contrast, mice infected with EBV showed 90% to 100% of the CD4$^+$ and CD8$^+$ T cells in lymphatic tissues expressing PD-1 (**Fig.5B, D, Supplemental Table S1**). Regarding absolute T cell numbers, mice with EBV-tumors showed twice as many PD-1$^+$ CD4$^+$ and three times as many CD8$^+$ T cells as infected mice without tumors (**Table 2, Fig.5C, E, Supplemental Table S1** SPL: control vs EBV; *P* = 0.91, control vs EBV-Tumor; *P* = 0.02, EBV vs EBV-Tumor; *P* = 0.06; LN: control vs EBV; *P* = 0.45, control vs EBV-Tumor; *P* = 0.0043, EBV vs EBV-Tumor; *P* = 0.07; BM: control vs EBV; *P* = 0.38, control vs EBV-Tumor; $P \leq 0.0001$, EBV vs EBV-Tumor; *P* = 0.0002).

Combined analyses of PD-1/ Tim-3 and PD-1/ CD69 expression by T cells from LN

To further characterize the activation and potential dysfunctional status of the T cells upon chronic EBV infection, the expression of PD-1 was examined in combination with Tim-3 or CD69 by multicolor flow cytometry analyses. Previously, double negative (DN) Tim-3$^-$PD-1$^-$ CD8$^+$ cytotoxic T lymphocytes (CTLs) were classified as functional CTLs, whereas single negative (SN) Tim-3$^-$PD-1$^+$ and double positive (DP) Tim-3$^+$PD-1$^+$ were previously defined to be "partially dysfunctional" and "severely dysfunctional", respectively [30]. Mononuclear cells obtained from lymph nodes of non-infected control mice (n=5), EBV-infected (n=5) and EBV-infected with tumor development (n=5) were analyzed in parallel. Similar to previous observations, compared with controls, all mice infected with EBV showed significantly higher frequencies of PD-1$^+$ CD4$^+$ and CD8$^+$ T cells **(Fig. 6A-B)**. A significant up-regulation of PD-1expression was observed for EBV-infected mice developing tumors (CD4$^+$ T cells: control vs EBV-Tumor; *P* = 0.002, EBV vs EBV-Tumor; *P* = 0.026; CD8$^+$ T cells: control vs EBV; *P* = 0.036, control vs EBV-Tumor; *P* = 0.013) **(Fig. 6A-B)**. Unlike PD-1, expression of the inhibitory receptor Tim-3 on CD4$^+$ T cells was comparable among all cohorts, both for cell frequencies and levels of expression **(Fig. 6C)**. In contrast, the frequency of Tim-3$^+$ CD8$^+$ T cells was three times higher for mice infected with EBV (without or with tumors) compared with controls, and this was also associated with up-regulation of Tim-3 expression **(Fig.6D)**. As a reference marker to assess T cell activation solely, CD69, a classical early marker of lymphocyte activation, was explored [31]. The frequency of CD69$^+$CD4$^+$ T cells was significantly lower for the cohort of mice developing tumors (40%) compared with controls (roughly 60%), and this was also associated with lower expression levels (control vs EBV-tumor; *P* = 0.024) **(Fig. 6E)**. On the other hand, CD69 expression on CD8$^+$ T cells was similar for all the cohorts **(Fig. 6F)**. These findings indicated that expression of the activation marker CD69 was uncoupled with the transcriptional program resulting into PD-1 up-regulation and symptomatic dysfunction. The analyses of the two co-inhibitory receptors Tim-3 and PD-1 was subsequently linked to define the functional status of T cells subjected to chronic stimulation with EBV antigens. A significant decrease was found in frequencies of the DN CD4$^+$ and CD8$^+$ Tim-3$^-$PD-1$^-$ functional T cell subpopulation upon EBV infection (CD4$^+$: control vs EBV; *P*= 0.004, control vs EBV-Tumor; *P* = 0.000; CD8$^+$: PD-1$^-$Tim-3$^-$: control vs EBV; $P \leq 0.0001$, control vs EBV-tumor; $P < 0.0001$) and a significant increase of the SN Tim-3$^-$PD-1$^+$ partially dysfunctional subpopulation for CD4$^+$ cells (control vs EBV; *P* = 0.004, control vs EBV-Tumor; *P* = 0.0002) **(Fig. 6G)**. Even more pronounced effects were observed for CD8$^+$ cells (control vs EBV; *P* = 0.0002, control vs EBV-Tumor; *P* = 0.0002) **(Fig. 6H)**. Severely dysfunctional DP Tim-3$^+$ PD-1$^+$ CD4$^+$ cells were rare, and comparable among all groups **(Fig. 6G)**. However, the frequencies of DP cells were substantially elevated for CD8$^+$ cells when mice were infected with EBV (> five-fold, frequency mean: control=2.068%; EBV=12.42%; EBV-Tumor=12.87%; although not statistically significant differences) **(Fig. 6H)**. For CD4$^+$ cells, Tim-3 expression level (Y axis) plotted relative to the PD-1 expression level (X axis) showed clustering of the mice developing tumors farther away from the other two cohorts **(Fig. 6G)**. When this analysis was applied to CD8$^+$ T cells, the non-infected cohort clustered clearly separately from the EBV infected and EBV with tumor cohorts **(Fig. 6H)**. In sum, based on these combined immune phenotypic analyses of Tim-3 and PD-1 expression, EBV infection conclusively affected the functionality of T cells, and this was more pronounced for CD8$^+$ T cells. Further, to examine whether functional responses against EBV-specific antigens were detectable, IFN-γ ELISpot analysis was performed. Mononuclear cells were obtained from three EBV-seropositive healthy human donors (HD, PBMC), three EBV-seronegative cord blood units (CB) and from three mice per cohort (using cryopreserved/thawed bone marrow samples). T cell responses against the EBV antigens EBNA3 (recombinant protein) and BZLF1 (recombinant protein and peptide pool) where not detectable for the CB negative control and validated for all positive control HD subjects **(Supplemental Figure S1)**. In contrast, only T cells from one EBV-infected mouse developing tumor showed a trustworthy T cell response **(Supplemental Figure S1)**. Despite the limitations of IFN-γ ELISpot assays applied to humanized mice, these results further ratified that although human T cells expanded dramatically after EBV infection and development of tumors in humanized mice, they seemed to be dysfunctional.

In situ ***analyses of EBV infection and extent of tumor spread in spleen***

Histopathological analyses of tissues and tumors were performed in 14 cases, arbitrarily selected to cover the full range of changes observed in the experimental setting. These cases represented four non-infected controls (188, 600, Z4, Z10), four EBV-infected humanized mice without visible tumors on macroscopic inspection (referred to as "EBV" 604, 615, 617, 1014), and six EBV-infected humanized mice with macroscopically visible loco-regional tumors in different organs (referred to as "EBV-Tumor" 187, 602, 1015, 1440, 1510, 1570). Microscopic evaluation showed different stages of predominantly perivascular spread of EBV infected cells. Non-infected control mice were used as reference **(Fig. 7A).** For display, four representative examples of EBV-infected mice, illustrating different grades of severity including: minimal presence of EBV-infected cells infiltrates and no visible macroscopic tumor (**Fig. 7B**), increased splenic perivascular spread of *EBER*-positive cells in cases with macroscopically visible tumors in a different location (**Fig. 7C**), splenic tumors that appeared to be progressive stages of increased perivascular spread of EBV positive lymphoproliferative neoplasia (**Fig. 7D**), and a necrotic large tumor in spleen, where the pre-existing murine splenic tissue and the spatially organized inflammatory reaction of human normally sized immune cells of T- and B-cell origin was almost completely replaced by the lymphoproliferative lesion (**Fig. 7E**), were chosen.

In situ *analyses of the inflammatory microenvironment in context of EBV infection*

In the representative cases corresponding to different grades of disease spread, the lymphoproliferative lesion was characterized by a consistent lymphoid blast–like morphology and frequent CD20/CD30 co-expression (**Fig. 7, 8**), and was associated with different densities of infiltrating CD3$^+$ T cells (**Fig. 8**). Further immunophenotyping of these T-cell infiltrates in close proximity to EBV-positive cells revealed variable numbers of CD8$^+$ and CD4$^+$ T cells, with a peak of CD8$^+$ cells in areas of high EBV density, and a striking co-localization of EBV–positive cells and the abundance of PD-1$^+$ cells (**Fig. 8**). This pattern was most obvious in splenic tissue. Nevertheless, human T cell infiltrations into kidney and liver showed similar trends. For example, co-localization of *EBER*-positive and CD20$^+$/CD30$^+$ blasts with CD3$^+$ and PD-1$^+$ cells was observed in a case of renal infiltration (**Fig. 9 A, B**), and in a different case where a similar constellation was present in liver tissue (**Fig. 9C**). Quantification of *EBER*$^+$ cells in perivascular regions of the spleen showed a trend towards increased levels of *EBER* detection in mice developing macroscopically detectable tumors although results were quite variable (**Fig. 10A, C and Supplemental Figure S2**). In sum, histopathology analysis complemented the analysis of homogenized tissues (analyzed by FACS) by clarifying the spatial distribution of infiltrating immune cells and by enabling spatially resolved subtyping *(***Fig. 10B, D**).

Discussion

In a previous study, Lee et al showed that the immune cell composition in long-term humanized mice played an important role in the development and shaping of EBV-induced B-cell lymphoma [19]. EBV-associated HL was seen exclusively in mice after long-term (15 weeks) human reconstitution and particularly upon co-implantation of mesenchymal stem cells expressing an active notch ligand DLK1, resulting in human CD3$^+$ T cell skewing. In this study, infections with EBV strains derived from the B95.8 virus and engineered to co-express reporter genes were performed at 15 to 17 weeks after huHSCT. Therefore, T cells were allowed to resume development and to be activated naturally by the EBV-infection and/or resulting tumorigenesis. Further, in this study, CD8$^+$ and CD4$^+$ T cell expansion was sequentially monitored in blood by longitudinal flow cytometry analyses, showing CD8$^+$ T lymphocytes vigorously expanding due to infection and particularly due to tumor development. In several lymphatic tissues, especially when tumor growth was observed (eg, spleen, lymph nodes), this resulted in a massive accrual in the absolute CD8$^+$ T cell numbers. Nevertheless, this enormous increase in the numbers of CTLs was unable to counteract tumor growth and may even support tumor development. This assumption was backed by high PD-1 expression on partially dysfunctional CD8$^+$ T cells and also detection of a Tim-3$^+$PD1$^+$ severely dysfunctional population, raising the possibility of blunted or even tumor-promoting immune responses. Histopathological analyses further highlighted that the PD-1$^+$ T cell–rich infiltrates and early manifestations of perivascular tumor spread co-localized, further supporting the notion of inefficient immune cell–tumor cell interactions that do not result in tumor clearance. Thus, in our work, tumor occurrence and extreme T-cell activation patterns confirmed the previously observed findings [19], but in contrast to Lee et al, who concluded that these EBV-induced tumors indeed resembled HL, this study provides evidence for a potential role of the extreme T-cell activation and dysfunctional CTL patterns co-developing with a highly malignant lymphoproliferative disease, resembling monomorphic PTLD or high-grade diffuse-large B-cell lymphoma (DL-BCL). These results rather go along with clinical findings obtained by Macedo et al from the analyses of asymptomatic pediatric thoracic organ transplant patients with high EBV load carriers, showing increased frequencies of EBV-specific CD8$^+$ T cells with CD38, PD-1, and CD127 up-regulation, features of cellular exhaustion [32]. These results pointed to the importance of chronic EBV load and of the levels of antigenic pressure in shaping EBV-specific memory CD8$^+$ T cells, underscoring the potential relevance of immunologic monitoring of EBV-specific CD8$^+$ T cells in the clinic. Indeed, a separate clinical study by Binger et al analysed asymptomatic patients who carried very high EBV viral loads over prolonged periods and concluded that this chronic high EBV load state was a predictor of *de novo* or recurrent PTLD [33]. Our combined results suggested that the brisk immunological response in humanized mice could support tumor seeding in peripheral organs and promote early phases of local tumor lesions. Using humanized NSG mice engrafted with human fetal bone marrow CD34$^+$ cells together with human thymus and liver (“BLT” model), other groups showed that the capacity of T cells to prevent EBV-related oncogenic transformation and to control growth of EBV-associated tumors derived from *in vitro* infected B cells was variable and could be modulated by therapeutic interventions [18], [34], [17], [35]. In another type of model, monoclonal antibodies blocking the T cell inhibitory receptors, PD-1 and CTLA-4, enhanced the ability of adoptive T cells selected from cord blood to control the EBV infection and the outgrowth of PD-L1$^+$/ PD-L2$^+$ lymphomas in mice challenged with cord blood B cells infected with EBV *in vitro* [36]. The main overall issue with these previous models is that the T cell reconstitution was weak and/or provided adoptively, not allowing the HLA-restricted immune editing process, ie, by which the immune suppressive TME could restrict productive anti-tumor immune responses. Further, the analyses of the human immune reconstitution was expanded to several lymphatic tissues (ie, including BM, mLN, and LN), systemic effects could be assessed. This may be important in mouse models testing new immune therapies to foresee organ-specific effects or toxicities. Another remarkable finding was the perivascular spread of PD-1^+ cells co-localizing with tumors. This is important from the clinical perspective, as the clinical effect can be potentially optimized if immune therapies could be delivered preferentially to highly vascularized tumor localizations. Further, innovative developments in non-invasive imaging and CT analyses could in the future provide precise and dynamic spatio-temporal information regarding the immune potency of novel therapies to subvert oncogenesis. In summary, in this work, we extended the analyses of humanized mice infected with EBV towards a fully endogenous, persistent, and dynamic co-development of tumors and T cells, ultimately leading to immune exhaustion whereby the tumors ultimately maintained the upper hand. In sum, this straightforward working model containing tumor and immune cells developing in mice from the same human subject reproduced clinical findings obtained in post-transplant patients and will be suitable to demonstrate preclinical proof-of-concept of novel immune therapies *in vivo*. A straight-forward validation would be to examine if this CTL dysfunctional phenotype can be rescued with an antibody therapy directed towards PD-1 in humanized mice infected with EBV as currently performed for tumor models.

Acknowledgments

We thank all members of the Regenerative Immune Therapies Applied Laboratory for their valuable contributions.

R.S. planned the project, designed experiments, obtained funding and regulatory approvals, enrolled collaborators, interpreted the data, wrote the second draft, and edited the final manuscript. S.D. and C.S. conducted experiments; analyzed data, performed the statistical analyses, and wrote the first manuscript draft. F.F. performed the histopathological analyses, generated figures, and edited the final manuscript. N.K. established and performed histopathological staining and *in situ* hybridization. B.E.V. assisted in the set up and conducted the ELISpot assays. M.A., R.Z, T.T., Y-F.A.C., and W.H. generated and produced the genetically modified EBV strains and edited the final manuscript. A.S., S.T., and A.C. assisted in preparation and analyses of humanized mice. S.L. and A.B. assisted with technical know-how for the CT analyses. CvK procured cord blood for generation of the humanized mice.

References

[1] Yarchoan M, Hopkins A, Jaffee EM: Tumor Mutational Burden and Response Rate to PD-1 Inhibition. N Engl J Med 2017, 377:2500-1.

[2] Ansell SM, Lesokhin AM, Borrello I, Halwani A, Scott EC, Gutierrez M, Schuster SJ, Millenson MM, Cattry D, Freeman GJ, Rodig SJ, Chapuy B, Ligon AH, Zhu L, Grosso JF, Kim SY, Timmerman JM, Shipp MA, Armand P: PD-1 blockade with nivolumab in relapsed or refractory Hodgkin's lymphoma. N Engl J Med 2015, 372:311-9.

[3] Walsh NC, Kenney LL, Jangalwe S, Aryee KE, Greiner DL, Brehm MA, Shultz LD: Humanized Mouse Models of Clinical Disease. Annu Rev Pathol 2017, 12:187-215.

[4] Audige A, Rochat MA, Li D, Ivic S, Fahrny A, Muller CKS, Gers-Huber G, Myburgh R, Bredl S, Schlaepfer E, Scherrer AU, Kuster SP, Speck RF: Long-term leukocyte reconstitution in NSG mice transplanted with human cord blood hematopoietic stem and progenitor cells. BMC Immunol 2017, 18:28.

[5] Pearson T, Shultz LD, Miller D, King M, Laning J, Fodor W, Cuthbert A, Burzenski L, Gott B, Lyons B, Foreman O, Rossini AA, Greiner DL: Non-obese diabetic-recombination activating gene-1 (NOD-Rag1 null) interleukin (IL)-2 receptor common gamma chain (IL2r gamma null) null mice: a radioresistant model for human lymphohaematopoietic engraftment. Clin Exp Immunol 2008, 154:270-84.

[6] Sundarasetty B, Volk V, Theobald SJ, Rittinghausen S, Schaudien D, Neuhaus V, Figueiredo C, Schneider A, Gerasch L, Mucci A, Moritz T, von Kaisenberg C, Spineli LM, Sewald K, Braun A, Weigt H, Ganser A, Stripecke R: Human Effector Memory T Helper Cells Engage with Mouse Macrophages and Cause Graft-versus-Host-Like Pathology in Skin of Humanized Mice Used in a Nonclinical Immunization Study. Am J Pathol 2017, 187:1380-98.

[7] Lang J, Kelly M, Freed BM, McCarter MD, Kedl RM, Torres RM, Pelanda R: Studies of lymphocyte reconstitution in a humanized mouse model reveal a requirement of T cells for human B cell maturation. J Immunol 2013, 190:2090-101.

[8] Harris DT, Badowski M: Long term human reconstitution and immune aging in NOD-Rag (-)-gamma chain (-) mice. Immunobiology 2014, 219:131-7.

[9] Hidalgo M, Amant F, Biankin AV, Budinska E, Byrne AT, Caldas C, Clarke RB, de Jong S, Jonkers J, Maelandsmo GM, Roman-Roman S, Seoane J, Trusolino L, Villanueva A: Patient-derived xenograft models: an emerging platform for translational cancer research. Cancer Discov 2014, 4:998-1013.

[10] Wang M, Yao LC, Cheng M, Cai D, Martinek J, Pan CX, Shi W, Ma AH, De Vere White RW, Airhart S, Liu ET, Banchereau J, Brehm MA, Greiner DL, Shultz LD, Palucka K, Keck JG: Humanized mice in studying efficacy and mechanisms of PD-1-targeted cancer immunotherapy. FASEB J 2017.

[11] Kutok JL, Wang F: Spectrum of Epstein-Barr virus-associated diseases. Annu Rev Pathol 2006, 1:375-404.

[12] Islas-Ohlmayer M, Padgett-Thomas A, Domiati-Saad R, Melkus MW, Cravens PD, Martin Mdel P, Netto G, Garcia JV: Experimental infection of NOD/SCID mice reconstituted with human CD34+ cells with Epstein-Barr virus. J Virol 2004, 78:13891-900.

[13] Shultz LD, Saito Y, Najima Y, Tanaka S, Ochi T, Tomizawa M, Doi T, Sone A, Suzuki N, Fujiwara H, Yasukawa M, Ishikawa F: Generation of functional human T-cell subsets with HLA-restricted immune responses in HLA class I expressing NOD/SCID/IL2r gamma(null) humanized mice. Proc Natl Acad Sci U S A 2010, 107:13022-7.

[14] Fujiwara S, Imadome K, Takei M: Modeling EBV infection and pathogenesis in new-generation humanized mice. Exp Mol Med 2015, 47:e135.

[15] Traggiai E, Chicha L, Mazzucchelli L, Bronz L, Piffaretti JC, Lanzavecchia A, Manz MG: Development of a human adaptive immune system in cord blood cell-transplanted mice. Science 2004, 304:104-7.

[16] Melkus MW, Estes JD, Padgett-Thomas A, Gatlin J, Denton PW, Othieno FA, Wege AK, Haase AT, Garcia JV: Humanized mice mount specific adaptive and innate immune responses to EBV and TSST-1. Nat Med 2006, 12:1316-22.

[17] Strowig T, Gurer C, Ploss A, Liu YF, Arrey F, Sashihara J, Koo G, Rice CM, Young JW, Chadburn A, Cohen JI, Munz C: Priming of protective T cell responses against virus-induced tumors in mice with human immune system components. J Exp Med 2009, 206:1423-34.

[18] Ma SD, Hegde S, Young KH, Sullivan R, Rajesh D, Zhou Y, Jankowska-Gan E, Burlingham WJ, Sun X, Gulley ML, Tang W, Gumperz JE, Kenney SC: A new model of Epstein-Barr virus infection reveals an important role for early lytic viral protein expression in the development of lymphomas. J Virol 2011, 85:165-77.

[19] Lee EK, Joo EH, Song KA, Choi B, Kim M, Kim SH, Kim SJ, Kang MS: Effects of lymphocyte profile on development of EBV-induced lymphoma subtypes in humanized mice. Proc Natl Acad Sci U S A 2015, 112:13081-6.

[20] Baer R, Bankier AT, Biggin MD, Deininger PL, Farrell PJ, Gibson TJ, Hatfull G, Hudson GS, Satchwell SC, Seguin C, et al.: DNA sequence and expression of the B95-8 Epstein-Barr virus genome. Nature 1984, 310:207-11.

[21] Palser AL, Grayson NE, White RE, Corton C, Correia S, Ba Abdullah MM, Watson SJ, Cotten M, Arrand JR, Murray PG, Allday MJ, Rickinson AB, Young LS, Farrell PJ, Kellam P: Genome diversity of Epstein-Barr virus from multiple tumor types and normal infection. J Virol 2015, 89:5222-37.

[22] Delecluse HJ, Hilsendegen T, Pich D, Zeidler R, Hammerschmidt W: Propagation and recovery of intact, infectious Epstein-Barr virus from prokaryotic to human cells. Proc Natl Acad Sci U S A 1998, 95:8245-50.

[23] Warming S, Costantino N, Court DL, Jenkins NA, Copeland NG: Simple and highly efficient BAC recombineering using galK selection. Nucleic Acids Res 2005, 33:e36.

[24] Skorupski K, Taylor RK: Positive selection vectors for allelic exchange. Gene 1996, 169:47-52.

[25] Wang S, Zhao Y, Leiby M, Zhu J: A new positive/negative selection scheme for precise BAC recombineering. Mol Biotechnol 2009, 42:110-6.

[26] Steinbruck L, Gustems M, Medele S, Schulz TF, Lutter D, Hammerschmidt W: K1 and K15 of Kaposi's Sarcoma-Associated Herpesvirus Are Partial Functional Homologues of Latent Membrane Protein 2A of Epstein-Barr Virus. J Virol 2015, 89:7248-61.

[27] Volk V, Reppas AI, Robert PA, Spineli LM, Sundarasetty BS, Theobald SJ, Schneider A, Gerasch L, Deves Roth C, Kloss S, Koehl U, von Kaisenberg C, Figueiredo C, Hatzikirou H, Meyer-Hermann M, Stripecke R: Multidimensional Analysis Integrating Human T-Cell

Signatures in Lymphatic Tissues with Sex of Humanized Mice for Prediction of Responses after Dendritic Cell Immunization. Front Immunol 2017, 8:1709.

[28] Salguero G, Daenthanasanmak A, Munz C, Raykova A, Guzman CA, Riese P, Figueiredo C, Langer F, Schneider A, Macke L, Sundarasetty BS, Witte T, Ganser A, Stripecke R: Dendritic cell-mediated immune humanization of mice: implications for allogeneic and xenogeneic stem cell transplantation. J Immunol 2014, 192:4636-47.

[29] Sukdolak C, Tischer S, Dieks D, Figueiredo C, Goudeva L, Heuft HG, Verboom M, Immenschuh S, Heim A, Borchers S, Mischak-Weissinger E, Blasczyk R, Maecker-Kolhoff B, Eiz-Vesper B: CMV-, EBV- and ADV-specific T cell immunity: screening and monitoring of potential third-party donors to improve post-transplantation outcome. Biol Blood Marrow Transplant 2013, 19:1480-92.

[30] Singer M, Wang C, Cong L, Marjanovic ND, Kowalczyk MS, Zhang H, Nyman J, Sakuishi K, Kurtulus S, Gennert D, Xia J, Kwon JYH, Nevin J, Herbst RH, Yanai I, Rozenblatt-Rosen O, Kuchroo VK, Regev A, Anderson AC: A Distinct Gene Module for Dysfunction Uncoupled from Activation in Tumor-Infiltrating T Cells. Cell 2016, 166:1500-11 e9.

[31] Cibrian D, Sanchez-Madrid F: CD69: from activation marker to metabolic gatekeeper. Eur J Immunol 2017, 47:946-53.

[32] Macedo C, Webber SA, Donnenberg AD, Popescu I, Hua Y, Green M, Rowe D, Smith L, Brooks MM, Metes D: EBV-specific CD8+ T cells from asymptomatic pediatric thoracic transplant patients carrying chronic high EBV loads display contrasting features: activated phenotype and exhausted function. J Immunol 2011, 186:5854-62.

[33] Bingler MA, Feingold B, Miller SA, Quivers E, Michaels MG, Green M, Wadowsky RM, Rowe DT, Webber SA: Chronic high Epstein-Barr viral load state and risk for late-onset posttransplant lymphoproliferative disease/lymphoma in children. Am J Transplant 2008, 8:442-5.

[34] Ma SD, Yu X, Mertz JE, Gumperz JE, Reinheim E, Zhou Y, Tang W, Burlingham WJ, Gulley ML, Kenney SC: An Epstein-Barr Virus (EBV) mutant with enhanced BZLF1 expression causes lymphomas with abortive lytic EBV infection in a humanized mouse model. J Virol 2012, 86:7976-87.

[35] Yajima M, Imadome K, Nakagawa A, Watanabe S, Terashima K, Nakamura H, Ito M, Shimizu N, Yamamoto N, Fujiwara S: T cell-mediated control of Epstein-Barr virus infection in humanized mice. J Infect Dis 2009, 200:1611-5.

[36] Ma SD, Xu X, Jones R, Delecluse HJ, Zumwalde NA, Sharma A, Gumperz JE, Kenney SC: PD-1/CTLA-4 Blockade Inhibits Epstein-Barr Virus-Induced Lymphoma Growth in a Cord Blood Humanized-Mouse Model. PLoS Pathog 2016, 12:e1005642.

Figure Legends

Figure 1: Epstein Barr virus (EBV) infection i.v. primarily targets the spleen and spreads systemically. A: Flow cytometry analyses of PD-L1 and PD-1 expression on lymphoblastoid cell lines (LCLs) generated using EBV/B95.8-GFP or EBV/B95.8-fLuc2. **B:** A schematic representation of experiments. Humanized mice were infected with 10^5 GRU of either EBV/B95.8-GFP or EBV/B95.8-fLuc2 15 weeks after huHSCT. Mice infected with EBV/B95.8-fLuc2 were longitudinally monitored for bio-distribution of EBV infection by optical imaging and CT analyses and mice infected with EBV/B95.8-GFP were regularly bled to monitor the dynamics of reconstitution of human lymphocytes. For both experimental set-ups, mice were euthanized 10 weeks after infection. **C:** Luciferase signal of three representative EBV/B95.8/fLu2c infected humanized mice generated with stem cells from different cord bloods is displayed in a 2D bioluminescence analysis in lateral view at weeks 1, 3, and 5 after infection. **D:** Quantification of the intensity of bioluminescence in the spleen region over the course of the experiment. **E:** 3D analysis five weeks after infection using IVIS SpectralCT and LiveImage. **F** *Ex vivo* optical imaging analysis of explanted tissues showing bioluminescence signals.

Figure 2: Dynamics of frequencies of human $CD45^+$ in peripheral blood and relative frequencies $CD19^+$ and $CD3^+$ lymphocytes within hCD45 cells. Results are shown for control, Epstein Barr virus (EBV), and EBV-Tumor cohorts and the bar graphs represent the data analyzed on week 6 post infection. Bars filled with white, grey, and black represent control, EBV, and EBV-Tumor cohorts, respectively. Examples displayed for control, EBV, and EBV-Tumor representative mice six weeks post infection, showing the gating strategy for the $CD45^+$ population in **A** and overall results and a bar graph each showing mean and

standard error of each group six weeks post infection in **B**. **C:** Exemplary results for $CD19^+$ and $CD3^+$ populations (gated in $CD45^+$). CD19 (**D**) and CD3 (**E**) (gated in $CD45^+$) over the course of the experiment and a bar graph each showing standard error of the mean of each group six weeks post infection. Six weeks post infection was chosen as a time point for statistical analyses as it best signaled the turning point of the dynamics in the lymphocyte population. $^*P < 0.05$, $^{**}P < 0.01$, $^{***}P < 0.001$ indicated in the bar graphs.

Figure 3: Dynamics of relative frequencies of human $CD4^+$ and $CD8^+$ lymphocytes in $hCD45^+$ cells of peripheral blood. Results are shown for control, Epstein Barr virus (EBV), and EBV-Tumor cohorts and the bar graphs represent the data analyzed on week 6 post infection. Bars filled with white, grey, and black represent control, EBV, and EBV-Tumor cohorts, respectively. **A:** Examples displayed for control, EBV, and EBV-Tumor representative mice six weeks post infection, showing the $CD4^+$ and $CD8^+$ populations (gated in $CD45^+$ $CD3^+$ T cells). CD4 (**B**) and CD8 (**C**) frequencies relative to human $CD45^+$ cells detected in mice over the course of the experiment and a bar graph each showing standard error of the mean of each group six weeks post infection. $^{**}P < 0.01$, $^{***}P < 0.001$ indicated in the bar graphs.

Figure 4: Endpoint analyses of the frequencies and absolute counts of human T lymphocytes in different tissues. Bars filled with white, grey, and black represent control, Epstein Barr virus (EBV), and EBV-Tumor cohorts, respectively. **A:** Frequencies of $CD3^+$, $CD4^+$, and $CD8^+$ in $CD45^+$ cells in peripheral blood are shown for control (n=19), EBV (n=11), and EBV-Tumor group (n=8). **B:** Mesenteric lymph nodes were analyzed as previously mentioned for control (n=11), EBV (n=8), and EBV-Tumor group (n=7). Splenocytes were recovered from mice, counted, stained, and analyzed as mentioned above.

Frequencies are depicted in **C** and absolute numbers in **D** for control (n=19), EBV (n=11), and EBV-Tumor animals (n=8). $CD3^+$, $CD4^+$, and $CD8^+$ frequencies in lymph nodes (**E**) and absolute cell numbers(**F**) for control group (n=18), EBV (n=11), EBV-Tumor (n=8). Frequencies (**G**) and absolute cell numbers (**H**) in bone marrow. Control group (n=19), EBV (n=11), EBV-Tumor (n=8). $*P < 0.05$, $**P < 0.01$, $***P < 0.001$ indicated in the graphs.

Figure 5: Endpoint analyses of frequencies and absolute counts of the $PD\text{-}1^+$ human T cells in different tissues. Bars filled with white, grey, and black represent control, Epstein Barr virus (EBV), and EBV-Tumor cohorts, respectively. **A:** Gating strategy for analyses of PD-1 expression on $CD4^+$ and for $CD8^+$ cells. **B:** Frequencies of $PD\text{-}1^+/CD4^+$ for spleen (SPL), lymph nodes (LN), mesenteric lymph nodes (MLN), bone marrow (BM), and blood (BL). **C:** Absolute cell numbers of $PD\text{-}1^+/CD4^+$ for spleen, lymph nodes, and bone marrow. **D:** Frequencies of $PD\text{-}1^+/CD8^+$ for spleen (SPL), lymph nodes (LN), mesenteric lymph nodes (MLN), bone marrow (BM), and blood (BL). **E:** Absolute cell numbers of $PD\text{-}1^+/CD4^+$ for spleen, lymph nodes, and bone marrow. The sample sizes per tissues are shown in **Supplemental Table S1**. $*P < 0.05$, $**P < 0.01$, $***P < 0.001$.

Figure 6: Single and combined analyses of frequencies of $CD4^+$ and $CD8^+$ and respective mean fluorescence intensities (MFI) of PD-1, Tim-3, and CD69 on T cells obtained from lymph nodes (n=5 mice per cohort of control, Epstein Barr virus (EBV)-infected mice and EBV-infected mice developing tumors). Analyses of PD-1 on $CD4^+$ (**A**) and $CD8^+$ (**B**) T cells. Analyses of Tim-3 on $CD4^+$ (**C**) and $CD8^+$ (**D**) T cells. Analyses of CD69 on $CD4^+$ (**E**) and $CD8^+$ (**F**) T cells. **G:** Combined analysis of $CD4^+$ T cells. Panel with bar graphs on the left depict combined analyses of PD-1 and Tim-3 ($Tim\text{-}3^-PD\text{-}1^-$ defined phenotypically as functional, $Tim\text{-}3^-PD\text{-}1^+$ defined as partially dysfunctional, $Tim\text{-}3^+PD\text{-}1^+$ defined as

severely dysfunctional). Panels with MFI for PD-1 (X axis) and MFI for Tim-3 (Y axis) showing relationship between expression levels of both markers for each cohort. **H:** Similar combined analysis for CD8$^+$ T cells. **P* < 0.05, ***P* < 0.01, ****P* < 0.001 indicated in the graphs.

Figure 7: Histopathological analysis of four exemplary samples of splenic tissue analyzing spread of Epstein Barr virus (EBV)-positive cells and formation of tumor. **(**HE, Giemsa, *EBER*, CD30; 10x objective in **A**, **B,** and **C**, 4x objective for **D** and **E**, 40x objective for all inserts). Arrows in EBER and CD30 panels indicate positive staining signals. **A:** Representative example for staining of spleen of an uninfected control humanized mouse. **B:** Detection of few EBV-positive cells in minimal perivascular spread (pvs) in the spleen (spl) in a representative example for the EBV-infected group without macroscopically detectable tumors. **C:** Representative example of splenic perivascular spread of EBV-positive and CD30-expressing cells in an animal that developed a macroscopically visible tumor elsewhere. **D:** Tumor (tu) formation of intermediate size in the spleen. Note the densely packed EBV-positive cells (as detected by *EBER* ISH) in the tumor area (tu), whereas the adjacent splenic tissue (spl) shows the previously described perivascular spread (pvs). **E:** Example of a large partially necrotic (nec) tumor. Pre-existing splenic tissue (spl), perivascular spread (pvs), tumor (tu), and necrotic regions (nec).

Figure 8: Histopathological analysis of representative samples of splenic tissue characterizing immune cell infiltration in context of Epstein Barr virus (EBV)-positive cell spread and tumor formation (Giemsa, *EBER*, CD20/CD3 duplex staining, CD8, CD4, and PD-1; 10x or 20x objective, 40x objective for all inserts). **A:** Representative staining of a spleen of an uninfected control humanized mouse. **B-D:** EBV-infected humanized mice. **B-E:**

Perivascular spread and tumor formation of EBV-infected cells was associated with a T-cell rich infiltrate. In cases with minimal perivascular spread **(B),** a few EBV-positive cells are mixed with presumably pre-existing B-cells in the humanized splenic microenvironment, and are surrounded by a moderate mixed T-cell infiltrate with low fractions of PD-1 positivity. In cases with more advanced perivascular spread (**C)** the infiltrates associated with the EBV-infected cells consist predominantly of T-cells, of both $CD4^+$ and $CD8^+$ phenotype, with increasing fractions of PD-1–expressing cells. $CD20^+$ cells in this microenvironment could be remnants of pre-existing splenic tissue, or invading CD20-expressing EBV infected cells. The case with an intermediate sized splenic tumor (**D)** shows massive perivascular spread of $CD20^+$ blasts, co-localizing with the EBV-positive cell population, and surrounded by PD-1^+ T-cells. The images show an area within the tumor formation, with strikingly low numbers of T-cells. The case with a large necrotic tumor **(E)** shows a more prominent T-cell infiltrate with substantial PD-1 expression. Pre-existing splenic tissue (spl), perivascular regions (pvs), tumor (tu), and necrotic regions (nec).

Figure 9: Histopathological analysis of extra-splenic spread in kidney and liver in the Epstein Barr virus (EBV)-infected tumor-bearing group. (HE, Giemsa, CD30, *EBER*, CD20, CD3, PD-1;10x objective in **A**, 20x objective in B and **C**, 40x objective for all inserts) Histopathological investigation reveals subtle tumor-like spread of EBV-positive blasts into several organs, of which staining of kidney tissue **(A, B)** and liver tissue **(C)** is shown as an example. On the right are examples of staining of the corresponding tissue of a non-infected control. Note that the automated EBER *in situ* hybridization produced some diffuse unspecific background staining (ubg) that was not nuclear and clearly distinguishable from specific nuclear staining by coloring and density. **A:** Multiple spread of tumors in the kidney is associated with blood vessels, and shows co-localization between *EBER* hybridization signal,

CD20^{+} cells with blast morphology, and PD-1–expressing T-cell infiltrates (arrows). **B:** Higher magnification reveals the morphology of an EBV-positive neoplasia of B-cell origin with CD30 expression in a majority of blast-like cells. It is accompanied by a dense infiltrate of PD-1 expressing cells. The pink arrow indicates a positive CD20 staining signal and the brown arrow a positive CD3 staining signal. **C:** A similar pattern can be observed in a different case, with mostly perivascular spread of a blast-like hematological neoplasia with CD20 and CD30 co-expression and an accompanying infiltrate containing PD-1–positive T-cells. The pink arrow indicates a positive CD20 staining signal and the brown arrow a positive CD3 staining signal.

Figure 10: Automated quantification of Epstein Barr Virus (EBV)**-infected cells and evaluation of stained image objects representing CD4, CD8, and PD-1 positive immune cells.** The quantitative assessment of EBV-positive cells in zones of perivascular spread ("EBV infected cells") and the estimation of immune cell infiltration ("Lymphocyte density") revealed strikingly variable infiltrates with a trend towards increased density of PD-1^{+} T-cells particularly in two cases (1440 and 1510) with a high perivascular load of EBV-infected cells. **A:** Representative example for perivascular spread of *EBER*-positive cells in an animal that developed macroscopically visible tumors elsewhere (1510). Left panel (40x objective): In the brightfield (original) images, the *EBER* –ISH positive cells are stained in dark blue. The false color images generated after deconvolution by multispectral imaging (MSI) highlight the detected positive nuclei in green. The result of the automated EBV cell detection (positive nuclei marked by blue dots) is shown in the insert of the original image. Right panel (10x objective in original, 20x objective in MSI images): PD-1 and CD4 immunohistochemistry showing perivascular accumulation of positive cells in the original image and after deconvolution by MSI. The result of automated quantification of image objects that

correspond to PD-1 and CD4 positive immune cells is shown in the insert of the MSI image. **B:** Corresponding image analysis in an EBV-infected case without macroscopically visible tumor burden shows few *EBER*-positive cells (617) , showing a moderate perivascular PD-1^+ infiltrate higher than in other cases without visible tumor load, but clearly lower than in the tumor-bearing cases 1510 and 1440. Asterisks: center of a blood vessel. **C:** The comparison between quantity of EBV-positive cells (left panel) and immune cell infiltrates confirming variability across different animals in both the tumor-free, and the tumor-bearing population.

Table 1: Mouse Characteristics.

Mouse ID	Sex	Cord blood ID	Group	hHSCT ID	CD45 %	EBV detection (qPCR/*EBER* ISH)	Tumors
601	M	263	Control	88	23,7	-/ND	Liver (mouse)
Z6	F	215	Control	95	68	-/ND	No
Z5	F	215	Control	95	41,7	-/ND	No
Z4	F	215	Control	95	55,8	-/ND	No
Z17	F	185	Control	96	42,7	-/ND	No
Z10	F	185	Control	96	47,5	-/ND	No
1481	F	272	Control	105	82	-/ND	No
1480	F	272	Control	105	75,3	-/ND	No
1062	F	229	Control	92	58,2	-/ND	No
1061	F	229	Control	92	33,5	-/ND	No
1060	F	229	Control	92	21,7	-/ND	No
618	M	195	Control	88	70,5	-/ND	No
616	M	153	Control	88	84,8	-/ND	No
603	F	212	Control	89	83,8	-/ND	No
600	F	212	Control	89	81,6	-/ND	No
582	M	264	Control	88	65,6	-/ND	No
188	F	230	Control	83	72,5	-/ND	No
12	F	222	Control	108	22,1	-/ND	No
2	F	222	Control	109	44,6	-/ND	No
1508	F	272	EBV	105	75	-/+	No
1469	F	147	EBV	104	61,7	+/ND	No
1391	F	147	EBV	104	66,2	+/ND	No
1016	F	229	EBV	92	16,1	+/ND	No
1014	F	229	EBV	92	25,7	+/+	No
617	M	195	EBV	88	72,9	+/+	No
615	M	153	EBV	88	72	+/+	No
606	F	212	EBV	89	82,7	-/+	No
605	F	212	EBV	89	76,9	+/ND	No
604	F	212	EBV	89	83,9	-/+	No
599	M	264	EBV	88	60,7	+/ND	No
1509	F	272	EBV-Tumor	105	83,8	-/+	SPL
1440	F	147	EBV-Tumor	104	49,3	+/+	SPL
3	F	222	EBV-Tumor	109	72,5	+/ND	SPL
1510	F	272	EBV-Tumor	105	79,4	+/+	SPL
602	M	263	EBV-Tumor	88	15,5	+/ND	SPL,KID, PA
1570	F	222	EBV-Tumor	108	77,7	+/ND	SPL, LIV
187	F	230	EBV-Tumor	83	50,9	+/+	SPL, LIV
1015	F	229	EBV-Tumor	92	50	+/+	SPL, KID, LIV

M-Male, F-female, ND-Not determined.

Table 2: Mean and standard deviation of the quantified absolute cell numbers obtained for spleen (CD45$^+$, CD3$^+$, CD19$^+$, CD8$^+$, CD4$^+$, CD8$^+$/PD-1$^+$, CD4$^+$/PD-1$^+$) and EBV DNA copies detected in spleen.

	Control (n=17) Mean±SD	**EBV (n=11) Mean±SD**	**EBV with tumor (n=6) Mean±SD**
CD45	8.615×10^6 $\pm 1.53 \times 10^7$	9.485×10^6 $\pm 6.458 \times 10^6$	2.022×10^7 $\pm 1.469 \times 10^7$
CD3	2.994×10^6 $\pm 5.729 \times 10^6$	6.759×10^6 $\pm 4.317 \times 10^6$	1.805×10^7 $\pm 1.380 \times 10^7$
CD19	4.994×10^6 $\pm 8.846 \times 10^6$	2.141×10^6 $\pm 2.767 \times 10^6$	1.347×10^6 $\pm 1.67 \times 10^6$
CD8	9.549×10^5 $\pm 1.996 \times 10^6$	3.415×10^6 $\pm 2.049 \times 10^6$	1.132×10^7 $\pm 8.366 \times 10^6$
CD4	1.973×10^6 $\pm 3.775 \times 10^6$	3.056×10^6 $\pm 2.456 \times 10^6$	6.191×10^6 $\pm 5.861 \times 10^6$
CD8+ PD-1+	9.719×10^5 $\pm 2.119 \times 10^6$	3.055×10^6 $\pm 1.985 \times 10^6$	8.941×10^6 $\pm 4.562 \times 10^6$
CD4+ PD-1+	1.772×10^6 $\pm 3.407 \times 10^6$	2.691×10^6 $\pm 2.21 \times 10^6$	5.384×10^6 $\pm 4.528 \times 10^6$
Copies/µg DNA	0 ± 0	9.420×10^2 $\pm 1.88 \times 10^3$	1.680×10^4 $\pm 2.7 \times 10^4$

Fig.1

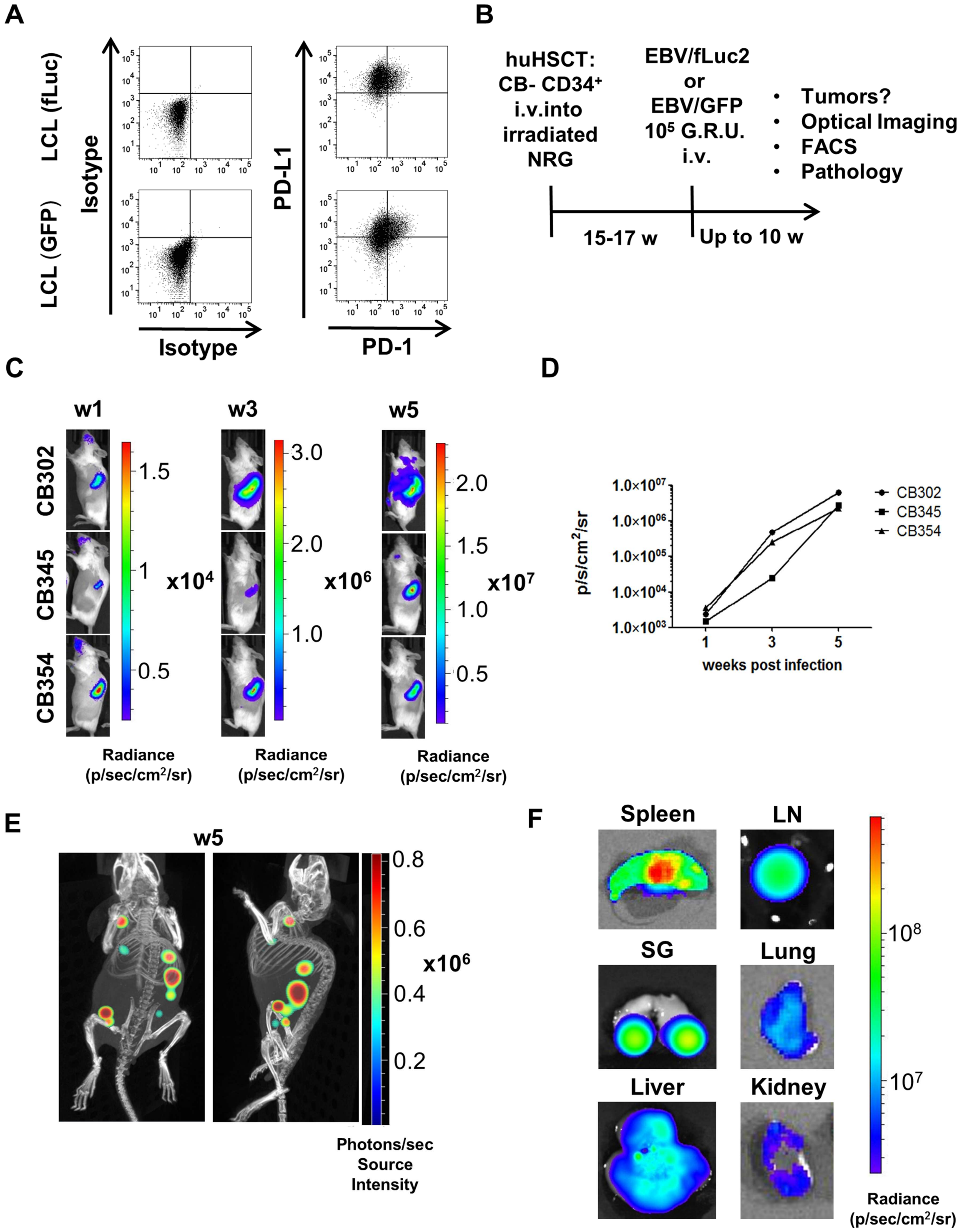
A
LCL (fLuc)
LCL (GFP)
Isotype
PD-L1
Isotype
PD-1
B
huHSCT:
CB- CD34+
i.v.into
irradiated
NRG
EBV/fLuc2
or
EBV/GFP
10⁵ G.R.U.
i.v.
Tumors?
Optical Imaging
FACS
Pathology
15-17 w
Up to 10 w
C
w1
w3
w5
CB302
CB345
CB354
x10⁴
x10⁶
x10⁷
Radiance (p/sec/cm²/sr)
D
p/s/cm²/sr
1.0×10⁰⁷
1.0×10⁰⁶
1.0×10⁰⁵
1.0×10⁰⁴
1.0×10⁰³
1
3
5
weeks post infection
CB302
CB345
CB354
E
w5
0.8
0.6
0.4
0.2
x10⁶
Photons/sec Source Intensity
F
Spleen
LN
SG
Lung
Liver
Kidney
10⁸
10⁷
Radiance (p/sec/cm²/sr)

Fig.2

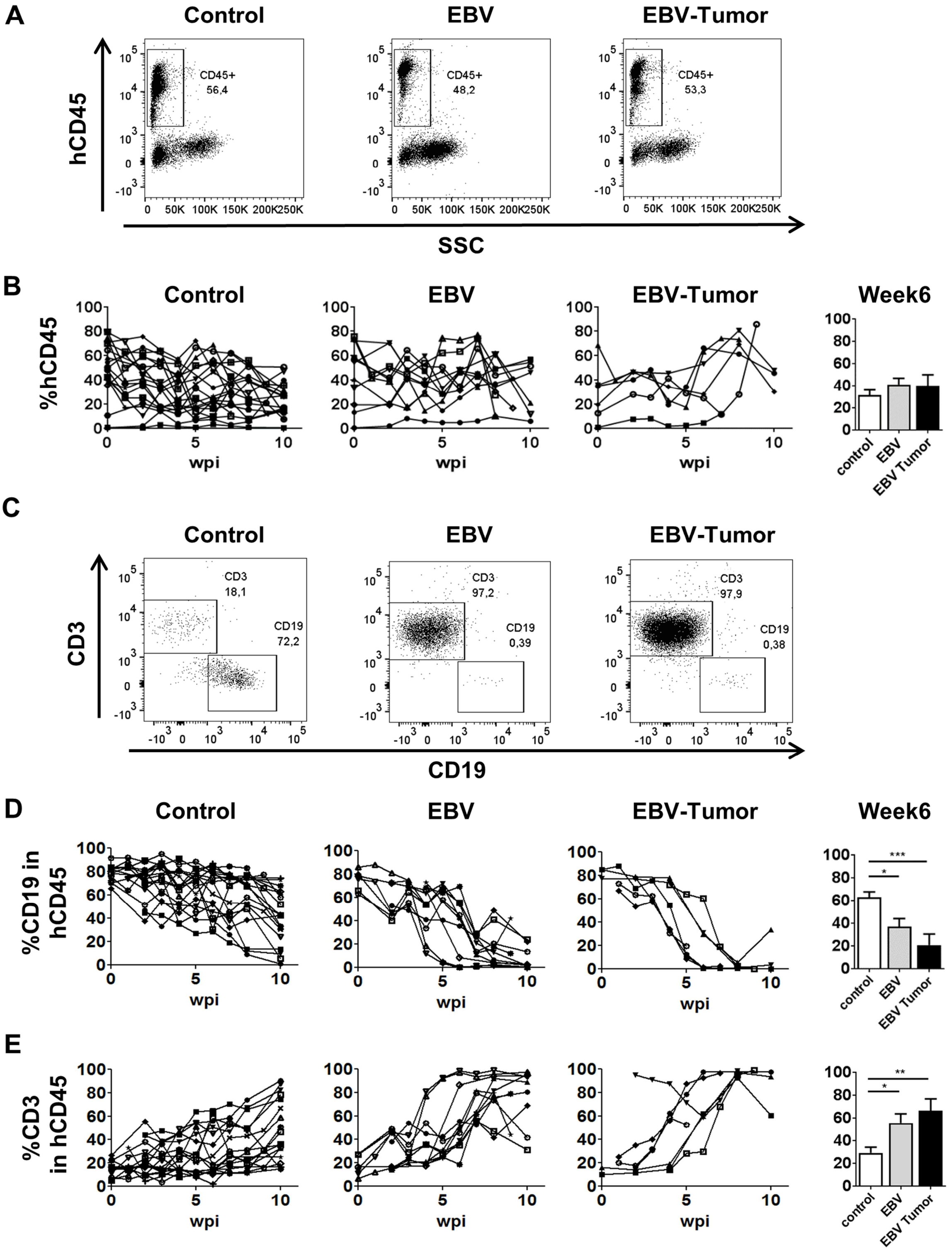
A
Control
EBV
EBV-Tumor
hCD45
CD45+
56,4
CD45+
48,2
CD45+
53,3
10^5
10^4
10^3
0
-10^3
0
50K
100K
150K
200K
250K
SSC
B
Control
EBV
EBV-Tumor
Week6
%hCD45
100
80
60
40
20
0
0
5
10
wpi
control
EBV
EBV Tumor
C
Control
EBV
EBV-Tumor
CD3
CD3
18,1
CD19
72,2
CD3
97,2
CD19
0,39
CD3
97,9
CD19
0,38
-10^3
0
10^3
10^4
10^5
CD19
D
Control
EBV
EBV-Tumor
Week6
%CD19 in hCD45
***
*
wpi
control
EBV
EBV Tumor
E
%CD3 in hCD45
**
*
wpi
control
EBV
EBV Tumor

Fig.3

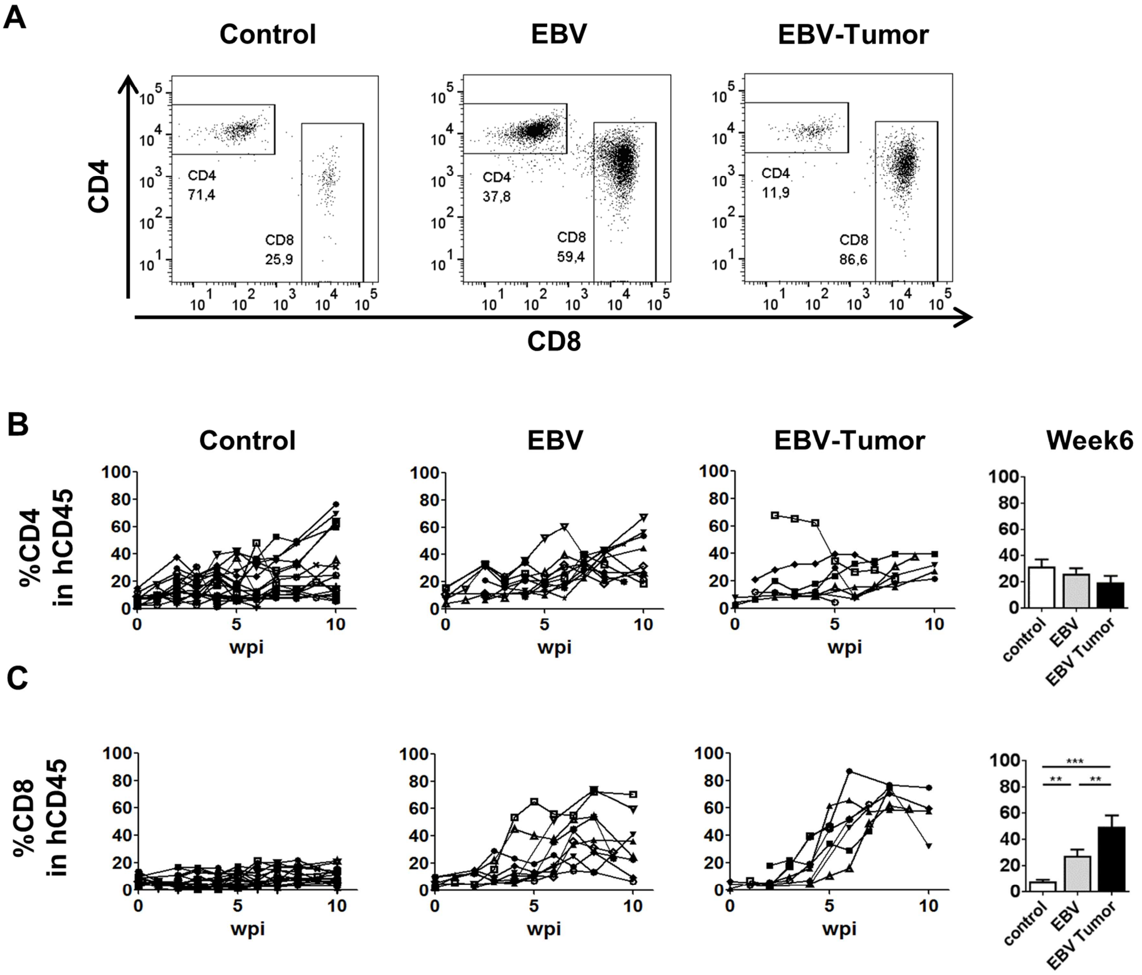
A
Control
EBV
EBV-Tumor
CD4
CD8
CD4 71,4
CD8 25,9
CD4 37,8
CD8 59,4
CD4 11,9
CD8 86,6
10^1 10^2 10^3 10^4 10^5
B
Control
EBV
EBV-Tumor
Week6
%CD4 in hCD45
wpi
0
5
10
0
20
40
60
80
100
control
EBV
EBV Tumor
C
%CD8 in hCD45
***
**
**

Fig. 4

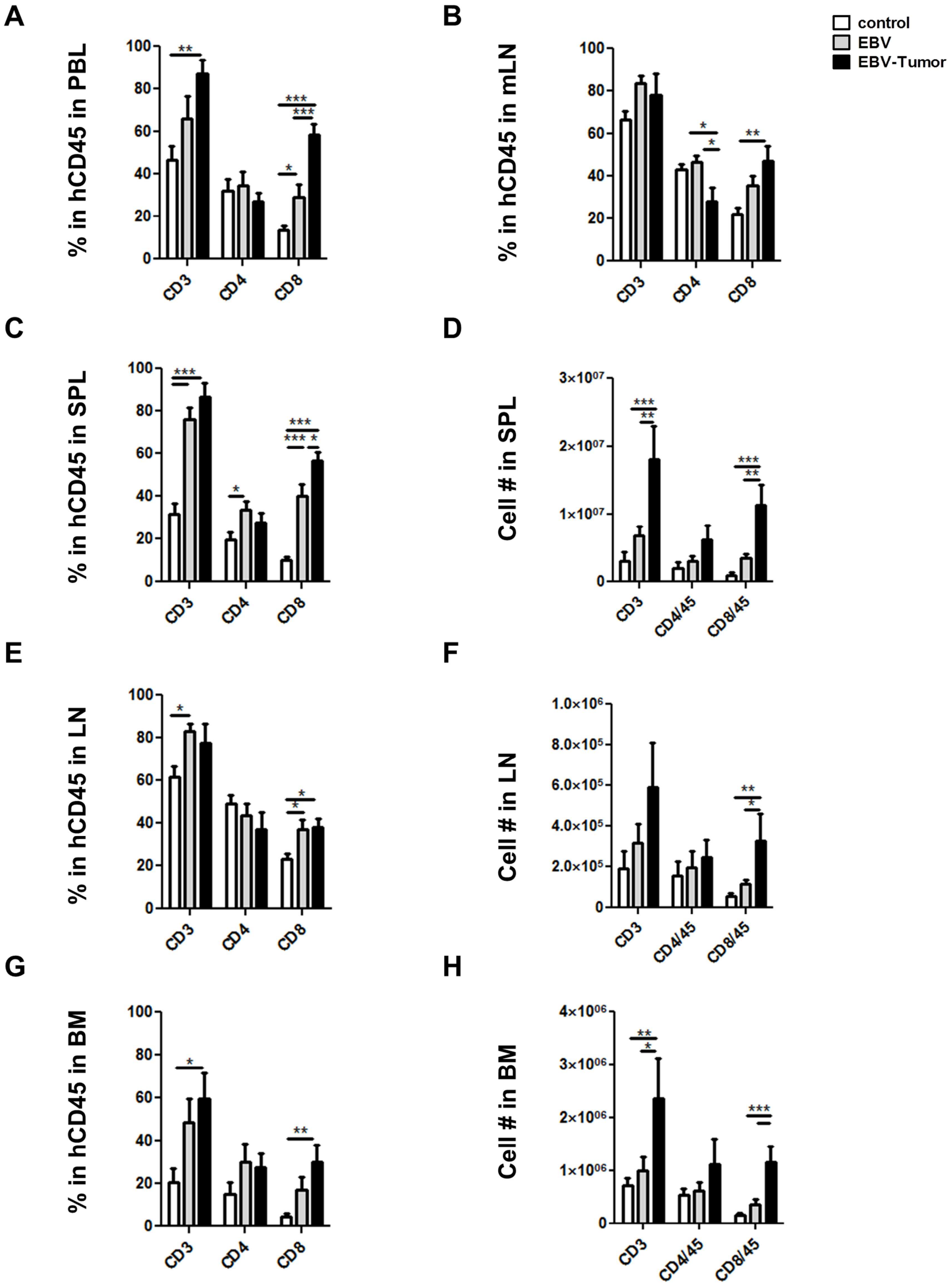
A
% in hCD45 in PBL
100
80
60
40
20
0
CD3
CD4
CD8
**
***
***
*
B
% in hCD45 in mLN
100
80
60
40
20
0
CD3
CD4
CD8
*
*
**
control
EBV
EBV-Tumor
C
% in hCD45 in SPL
100
80
60
40
20
0
CD3
CD4
CD8
***
*
***
*** *
D
Cell # in SPL
3×10⁰⁷
2×10⁰⁷
1×10⁰⁷
0
CD3
CD4/45
CD8/45
***
**
***
**
E
% in hCD45 in LN
100
80
60
40
20
0
CD3
CD4
CD8
*
*
*
F
Cell # in LN
1.0×10⁶
8.0×10⁵
6.0×10⁵
4.0×10⁵
2.0×10⁵
0
CD3
CD4/45
CD8/45
**
*
G
% in hCD45 in BM
100
80
60
40
20
0
CD3
CD4
CD8
*
**
H
Cell # in BM
4×10⁰⁶
3×10⁰⁶
2×10⁰⁶
1×10⁰⁶
0
CD3
CD4/45
CD8/45
**
*
***

Fig. 5

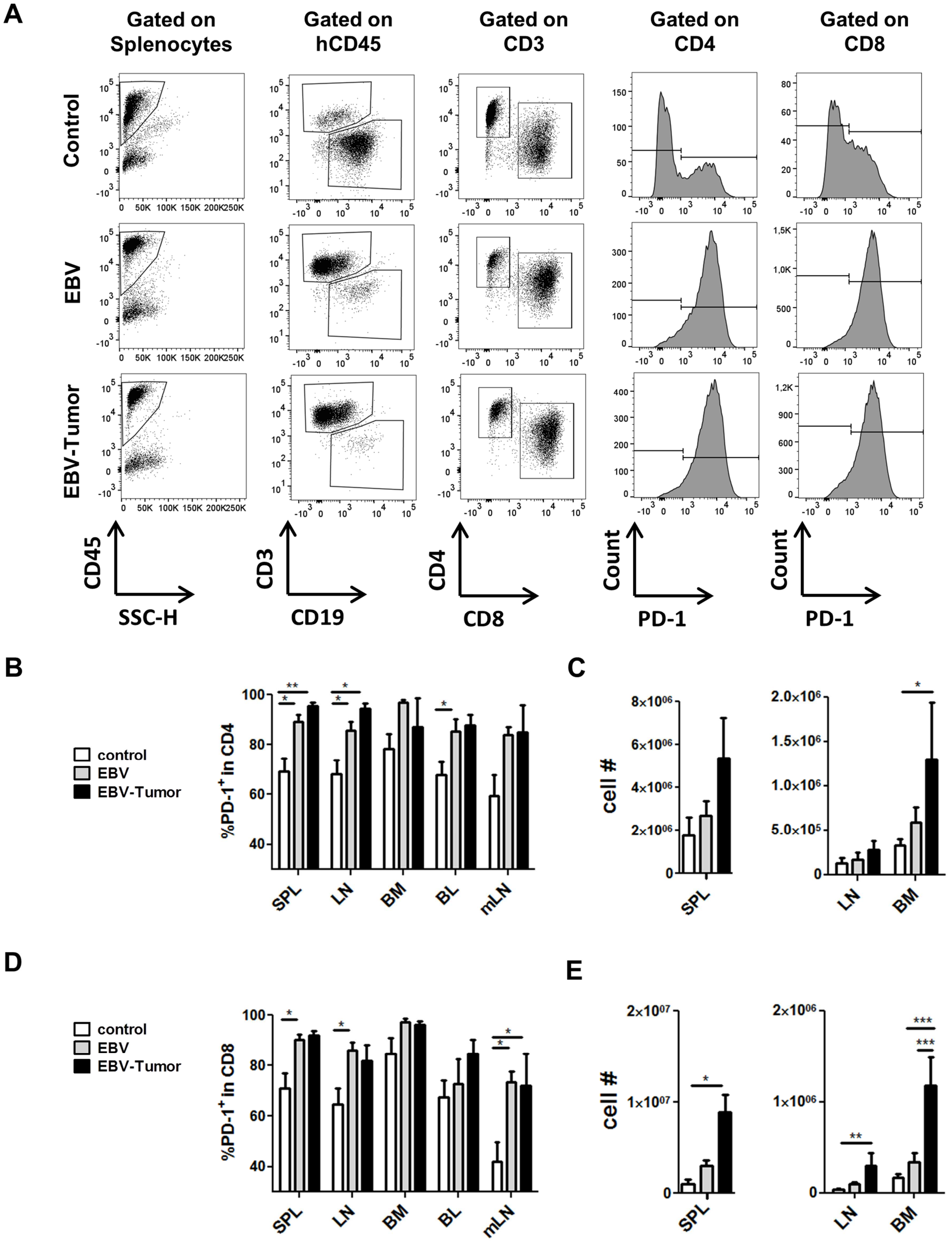
A
Gated on Splenocytes
Gated on hCD45
Gated on CD3
Gated on CD4
Gated on CD8
Control
EBV
EBV-Tumor
CD45
SSC-H
CD3
CD19
CD4
CD8
Count
PD-1
Count
PD-1
0
50K
100K
150K
200K
250K
150
100
50
80
60
40
20
300
200
1,5K
1,0K
500
400
1,2K
900
600
B
control
EBV
EBV-Tumor
%PD-1+ in CD4
100
80
60
40
SPL
LN
BM
BL
mLN
*
**
C
cell #
8×10⁰⁶
6×10⁰⁶
4×10⁰⁶
2×10⁰⁶
0
SPL
2.0×10⁶
1.5×10⁶
1.0×10⁶
5.0×10⁵
0
LN
BM
D
control
EBV
EBV-Tumor
%PD-1+ in CD8
100
80
60
40
SPL
LN
BM
BL
mLN
E
cell #
2×10⁰⁷
1×10⁰⁷
0
SPL
2×10⁰⁶
1×10⁰⁶
0
LN
BM
***
**

Fig. 6

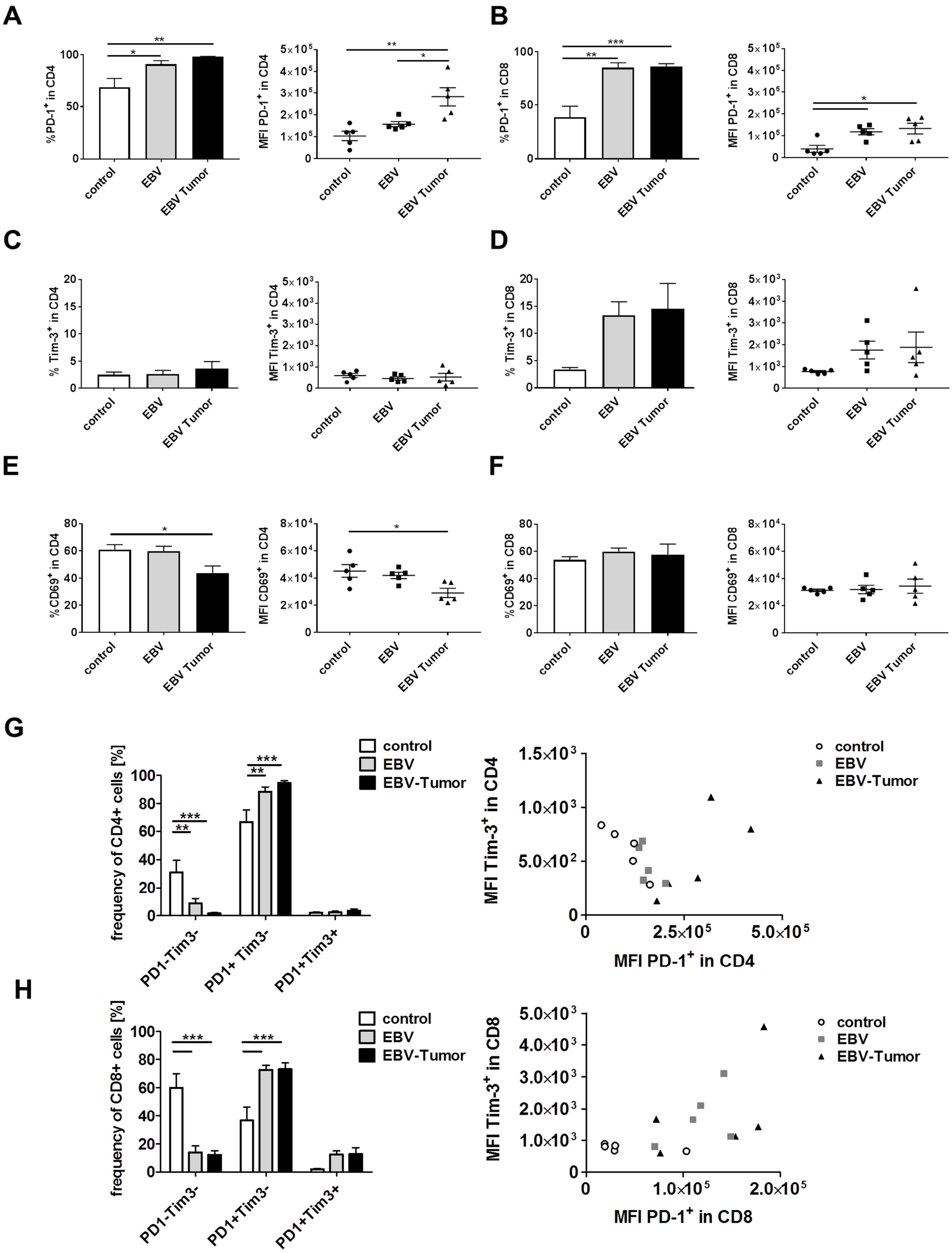
A
% PD-1+ in CD4
MFI PD-1+ in CD4
B
% PD-1+ in CD8
MFI PD-1+ in CD8
C
% Tim-3+ in CD4
MFI Tim-3+ in CD4
D
% Tim-3+ in CD8
MFI Tim-3+ in CD8
E
% CD69+ in CD4
MFI CD69+ in CD4
F
% CD69+ in CD8
MFI CD69+ in CD8
control
EBV
EBV Tumor
G
frequency of CD4+ cells [%]
PD1-Tim3-
PD1+ Tim3-
PD1+Tim3+
MFI Tim-3+ in CD4
MFI PD-1+ in CD4
H
frequency of CD8+ cells [%]
PD1-Tim3-
PD1+Tim3-
PD1+Tim3+
MFI Tim-3+ in CD8
MFI PD-1+ in CD8
control
EBV
EBV-Tumor
*
**
***

Fig. 7

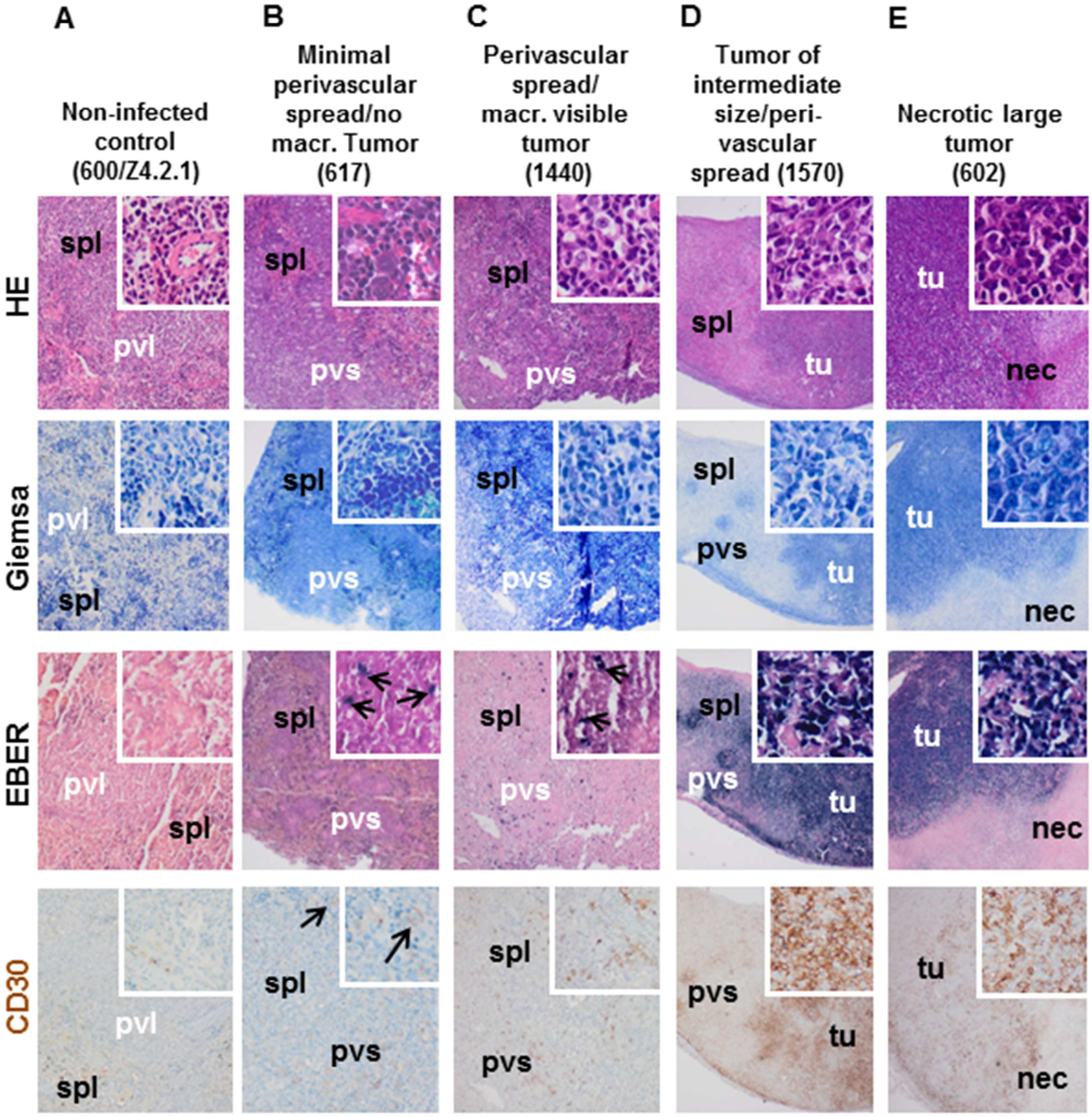
A
B
C
D
E
Non-infected control (600/Z4.2.1)
Minimal perivascular spread/no macr. Tumor (617)
Perivascular spread/ macr. visible tumor (1440)
Tumor of intermediate size/peri-vascular spread (1570)
Necrotic large tumor (602)
HE
Giemsa
EBER
CD30
spl
pvl
pvs
tu
nec

Fig. 8

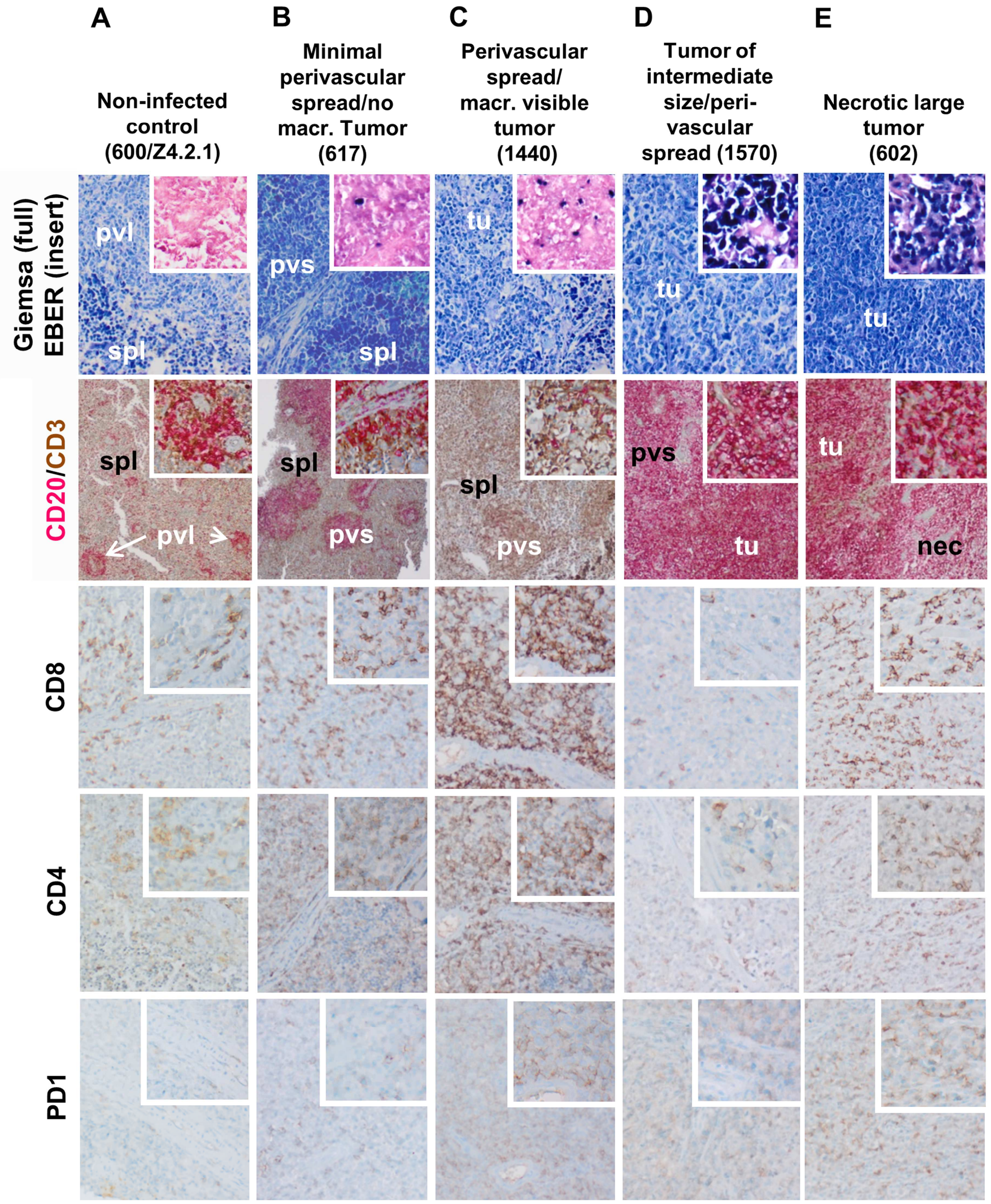
A
Non-infected control (600/Z4.2.1)
B
Minimal perivascular spread/no macr. Tumor (617)
C
Perivascular spread/ macr. visible tumor (1440)
D
Tumor of intermediate size/peri-vascular spread (1570)
E
Necrotic large tumor (602)
Giemsa (full) EBER (insert)
CD20/CD3
CD8
CD4
PD1
pvl
spl
pvs
spl
tu
tu
tu
spl
pvl
spl
pvs
spl
pvs
pvs
tu
tu
nec

Fig. 9

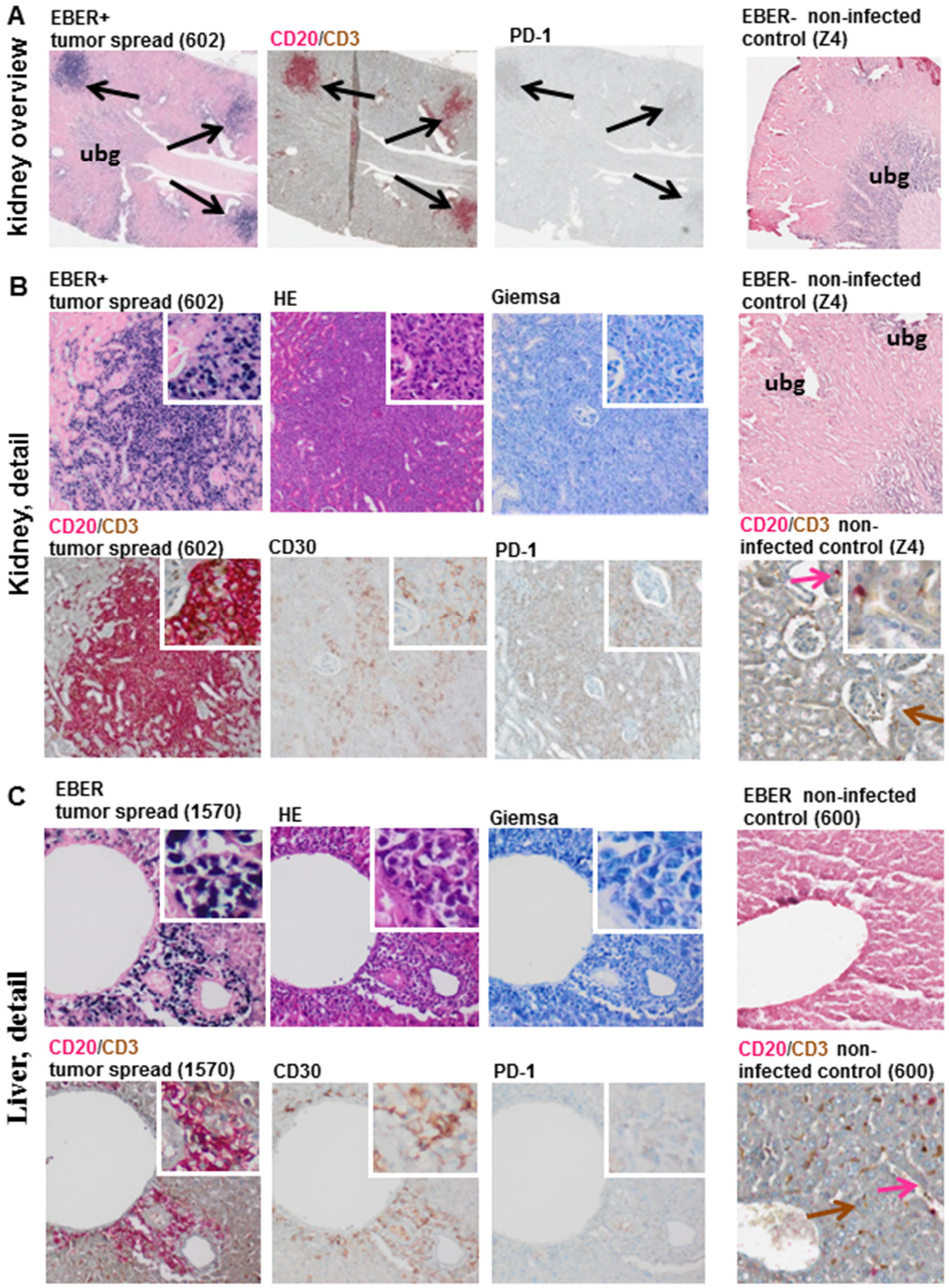
A
kidney overview
EBER+
tumor spread (602)
ubg
CD20/CD3
PD-1
EBER- non-infected
control (Z4)
ubg
B
Kidney, detail
EBER+
tumor spread (602)
HE
Giemsa
EBER- non-infected
control (Z4)
ubg
ubg
CD20/CD3
tumor spread (602)
CD30
PD-1
CD20/CD3 non-
infected control (Z4)
C
Liver, detail
EBER
tumor spread (1570)
HE
Giemsa
EBER non-infected
control (600)
CD20/CD3
tumor spread (1570)
CD30
PD-1
CD20/CD3 non-
infected control (600)

Fig. 10

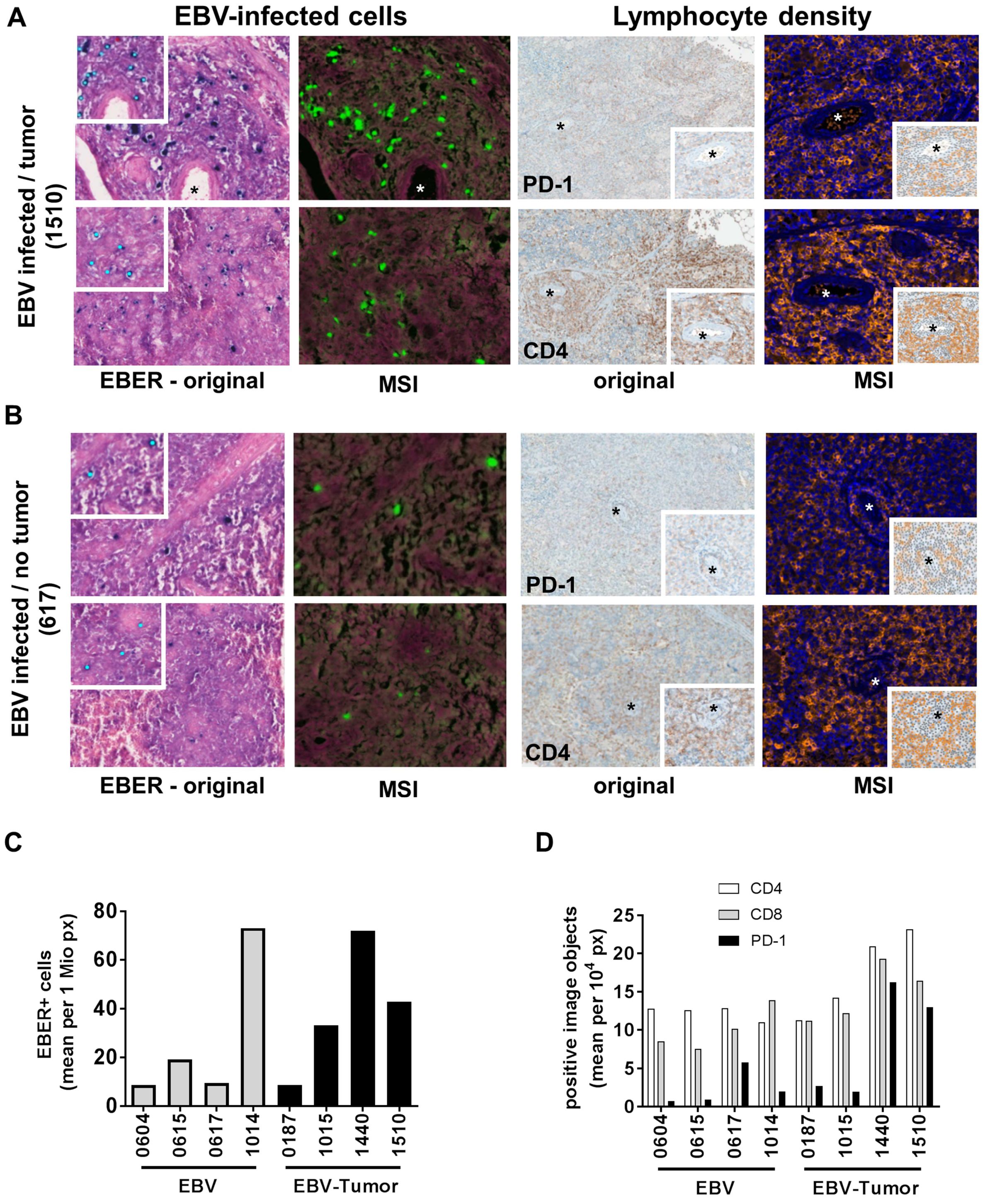
A
EBV-infected cells
Lymphocyte density
EBV infected / tumor
(1510)
PD-1
CD4
EBER - original
MSI
original
MSI
B
EBV infected / no tumor
(617)
PD-1
CD4
EBER - original
MSI
original
MSI
C
EBER+ cells
(mean per 1 Mio px)
0
20
40
60
80
0604
0615
0617
1014
0187
1015
1440
1510
EBV
EBV-Tumor
D
CD4
CD8
PD-1
positive image objects
(mean per 10^4 px)
0
5
10
15
20
25
0604
0615
0617
1014
0187
1015
1440
1510
EBV
EBV-Tumor